JM PAPERS

Thermal effect in shock-induced gas filtration through porous media

Jiarui Li[1,2], Jun Chen[1], Baolin Tian[3], Meizhen Xiang[1] and Kun Xue[2],†

[1]National Key Laboratory of Computational Physics, Institute of Applied Physics and Computational Mathematics, Beijing 100088, PR China

[2]State Key Laboratory of Explosive Science and Technology, Beijing Institute of Technology, Beijing 100081, PR China

[3]School of Aeronautic Science and Engineering, Beihang University, Beijing 100191, PR China

The gas dynamics of shock-induced gas filtration through densely packed granular columns with vastly varying shock intensity and the structural parameters are numerically investigated using a coupled Eulerian–Lagrangian approach. The results shed fundamental light on the thermal effects of the shock-induced gas filtration manifested by a distinctive self-heating hot gas layer traversing the medium. The characteristics of the thermal effects in terms of the thermal intensity and uniformity are found to vary with the shock Mach number, M_s, and the filtration coefficient of the granular media, Π. As the incident shock transitions from weak to strong, and (or) the filtration coefficient increases from $O(10^{-5})$ to $O(10^4)$, the heating mechanisms transition between three distinct heating modes. A phase diagram of heating modes is established on the parameter space (M_s, Π), which enables us to predict the characteristics of the thermal effect in different shock-induced gas filtrations. The thermal effects markedly accelerate the pressure diffusion due to the additional heat influx when the time scale of the former is smaller than or comparable to the latter. Based on the contour map displaying the coupling degree of the thermal effects and the pressure diffusion, we identify a decoupling criterion whereby the isothermal assumption holds if only the pressure diffusion is concerned. The thermal effects may well bring about considerable thermal shocks which pose a great threat to the integrity of the solid skeleton and further reduce the overall shock resistance performance of the porous media.

Key words: particle/fluid flow, shock waves, gas dynamics

1. Introduction

Flow in porous media has numerous applications in environmental protection, including groundwater mitigation (Bear & Alexander 2010; Pathak & Singh 2015; Eriksen *et al.*

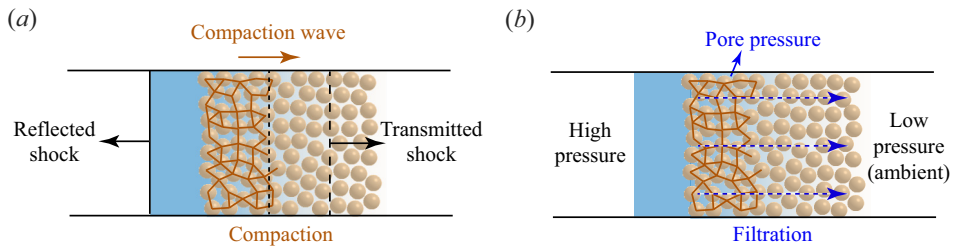† Email address for correspondence: xuekun@bit.edu.cn

Figure 1. Schematic diagrams of the two fundamental processes involved in the interaction of shock waves with porous media. (*a*) Compaction of the solid phase. (*b*) Gas filtration within the pores.

2018; Xue *et al.* 2019; Flekkøy, Sandnes & Måløy 2023), underground contaminant transport (Hayek 2017; Shen *et al.* 2023), carbon capture and geological sequestration (Abidoye, Khudaida & Das 2015; De Paoli, Zonta & Soldati 2016). In contrast to the aforementioned applications characterized by relatively low speed, the primary focus of this paper is on the phenomenon of shock-induced interstitial flow. Blast waves generated through the detonation of high explosives pose a serious hazard to individuals and structures in close proximity. Therefore, the mitigation of blast waves is a crucial practical concern (Britan *et al.* 2001; Ji, Li & Chen 2012; Frost 2018; Gubin 2018; Pontalier *et al.* 2018). Numerous porous media, such as granular material or aqueous foam, have been utilized as protective screens to mitigate blast energy (Skews 2001; Smith 2010; Petel *et al.* 2011; Britan *et al.* 2013; Del Prete *et al.* 2013; Vivek & Sitharam 2019). The head-on collision of normal shock waves with porous materials has been extensively studied as a prototype to investigate blast mitigation mechanisms, thereby garnering considerable attention in past decades (Gvozdeva, Faresov & Fokeev 1985; Henderson *et al.* 1990; Skews 1991; Ben-Dor *et al.* 1994).

The interactions of shock waves with porous media consist of two fundamental processes (Ben-Dor *et al.* 1997; Skews 2001; Yin *et al.* 2019; Han, Xue & Bai 2021; Li *et al.* 2023), as shown in figure 1. One is the intricate interaction between the transmitted wave and the skeleton of porous media. As particles constituting the porous medium move under the impact of shock waves, the contact among the particles increases, leading to a more densely packed medium. This phenomenon is referred to as compaction. During compaction, the solid stress propagates through contacts between particles, forming a compaction wave within the skeleton. The local particle volume fraction increases as the compaction front passes. The other involves gas penetration driven by a significant pressure difference between the reflected shock upstream and the ambient air downstream. This phenomenon, referred to as filtration in the literature, leads to an increase in the gas pressure within the pores, which is abbreviated as pore pressure (Britan *et al.* 1997). Since the transmitted wave rapidly decays during propagation, particularly in granular materials with low porosity, the compaction wave and gas filtration in long porous media with low to moderate porosities are of major concern (Rogue *et al.* 1998; Sadot *et al.* 2013). For flexible aqueous foams (polyurethane or polyethylene) or loosely packed granular materials, an interaction between the compaction wave and gas filtration is observed (Skews *et al.* 1992; Levy *et al.* 1993). Our previous study demonstrated that the presence of a fast-advancing compaction front would produce a deflection in the spatial distribution of the pore pressure due to the reduction in porosity (Li *et al.* 2023). The drag force exerted between the two phases involved in gas filtration would subsequently alter the compaction process (Ben-Dor *et al.* 1997; Xue *et al.* 2023). However, the compaction is minimal for rigid or densely packed granular materials, where the solid skeleton can be assumed to be

motionless (Rogg *et al*. 1985; Ram & Sadot 2015). In this scenario, the shock–particle interaction is solely determined by gas filtration through granular media.

Many experimental and numerical studies have been published on the topic of shock-induced gas filtration through rigid porous media. The experiments are typically carried out in vertical shock tubes, with the pressure history being measured by transducers mounted along the sidewalls and end wall. The objectives of these studies were to investigate the impact of shock strength, porosity, particle size and propagation distance on gas pressure. Due to the limited availability of the pressure transducers, a continuous pressure evolution law is difficult to establish. As a result, quantitative conclusions are derived by fitting limited pressure profiles. Experiments provide qualitative trends at the macroscale, but they do not capture microscale information such as local flow velocity or porosity changes. Therefore, numerical simulations provide a promising approach to investigate gas filtration and determine the underlying mechanism.

Notable progress was made by Morrison in his endeavour to mathematically describe the gas filtration induced by a nuclear underground explosion (Morrison 1972). In Morrison's approach, the pressure gradient in the filtration flow, denoted as $\partial P / \partial x$, depends on the interstitial gas velocity $\tilde{V}$ in a generalized form that is commonly known as the Forchheimer resistance law (Lage 1998):

$$\frac{\partial P}{\partial x} = -a\mu\tilde{V} - b\rho\tilde{V}|\tilde{V}|. \tag{1.1}$$

The first term on the right-hand side of (1.1) is called the Darcy term $-a\mu\tilde{V}$, and it accounts for viscous losses where μ is the gas viscosity. The Darcy coefficient, a, is related to the permeability, k, and porosity, ε, by the equation $a = \varepsilon/k$. The second term is the Forchheimer term $-b\rho\tilde{V}|\tilde{V}|$, where ρ is the gas density and b is the Forchheimer coefficient, and this term models the inertial loss. A non-dimensional parameter, the effective Reynolds number, Re_f, has been introduced to quantify the relative significance of these two terms. Gas filtration with $Re_f < 1$ and $Re_f \to \infty$, where the Forchheimer/Darcy term becomes negligible, was specified as Darcy-flow and Forchheimer-flow domains, respectively. Both Darcy flow and Forchheimer flow exhibit self-similar solutions for the pore pressure field, albeit with different scaling laws. Following Morrison's approach, Britan *et al*. introduced the thresholds of Re_f for classifying various flow regimes (including Darcy flow, Forchheimer flow and mixed flow between) based on the Mach number of the incident shock (Britan, Shapiro & Ben-Dor 2007). In addition, a hybrid method was developed to determine the values of the Darcy and Forchheimer coefficients (a and b) via controlled shock tube experiments and then enabled reconstruction of the pressure profiles at different locations within a granular sample (Britan *et al*. 2006).

The self-similar solution obtained from the Morrison approach requires steady boundary conditions, specifically maintaining the upstream pressure after the shock wave reflects off the front surface of the porous column, P_5, unchanged. The aforementioned requirements are barely met in shock tube experiments due to multiple reflections and complex wave interactions that occur within the porous column and in field tests. Hence, the Morrison method was modified by incorporating an unsteady upstream pressure as a boundary condition, based on the experimental data (Britan *et al*. 2006). The Morrison approach, which is relatively simplified, showed performance comparable to that of the full solution based on the complete system of conservation equations in accurately reproducing the pressure histories in the shock-impacted granular columns (Britan *et al*. 2006).

Although Morrison's model and its variants have the capability to simulate the transient pressure diffusion of gas filtration through granular columns, they do not incorporate the

thermodynamic evolution of interstitial flow. The flow temperature was considered to be equivalent to that of the solid phase, with both maintaining ambient temperature. This isothermal assumption becomes problematic as the intensity of the shock increases. Since the temperature of the upstream reflected shock, T_5, is dependent on the shock intensity, the gases upstream experience significant heating. In addition to the temperature difference between the upstream surface and that inside porous media, the compressible nature of the gas infiltration enables the exchange of kinetic energy and internal energy, indicating that the kinematic and thermodynamic parameters are interdependent during gas filtration. Evidently, the isothermal assumption is invalid in scenarios involving strong shock waves. Therefore, the applicability of the Morrison approach needs to be revisited. Although some full numerical methods considering the energy conversion of the flow have been employed in gas infiltration research in recent years, the majority of these studies focus on the relationship between the pressure evolution and initial parameters such as shock intensity, porosity and particle size. The fundamental question of the extent to which the thermodynamic evolution of gases influences the flow parameters of the shock-induced gas filtration remains unresolved.

The primary objective of this study is to gain insight into the thermal effect in shock-induced gas filtration and to determine the correlation between the thermodynamic and dynamic parameters. Full solutions consisting of the mass, momentum and energy conservation equations are viable options for accessing the potential thermal effect. Some of the full solutions treat both the gas and solid phases as a continuum, suggesting that the average flow parameters are minimally affected by local heterogeneity (Baer & Nunziato 1986; Petitpas *et al.* 2007; Saurel *et al.* 2017). Moreover, the gas flow velocity is assumed to be low such that the unsteady effects are minimal (Crowe *et al.* 2012). Evidently, these assumptions cannot universally hold in granular media composed of randomly packed particles with vastly varying sizes. To overcome these constraints, the discrete-element method (Patankar & Joseph 2001; O'Rourke & Snider 2010; Snider *et al.* 2011; Balachandar 2012; Alobaid & Epple 2013; Guo *et al.* 2015; Mo *et al.* 2019; Jiang *et al.* 2021; Qiao *et al.* 2022) is employed to generate a solid skeleton with particle-scale randomness. By coupling compressible computational fluid mechanics and the discrete-element method, referred to as CMP-PIC in our previous publications (Tian *et al.* 2020), we can consider the flow variation at the particle scale and conduct parametric studies on the variables relevant to the granular assembly.

In the following, brief accounts of CMP-PIC and the Morrison approach are presented in § 2. The numerical set-up is provided in § 3. The dynamics of the flow parameters during shock-induced gas filtration is described in § 4.1. The thermal effects characterized by the spatiotemporal evolution of the thermodynamic parameters are analysed in § 4.2. The mechanisms governing thermal effects and their influences on the flow parameters are discussed in § 4.3. The different domains of the thermal effects are defined in § 4.4, and the phase diagram is established in the parameter space comprising two essential non-dimensional parameters. The implications of thermal effects on granular media as protective shields, as well as the validity of the isothermal assumption for shock-induced gas infiltration, are discussed in § 5. A brief summary is provided in § 6.

2. Methods

2.1. *The CMP-PIC approach*

Numerical simulations were performed based on CMP-PIC, a coarse-grained Euler–Lagrange approach suitable for gas–particle flows in laboratory-scale systems

(Sundaresan *et al.* 2018; Koneru *et al.* 2020). The CMP-PIC approach tracks and accounts for contact interactions between parcels. Each parcel consists of multiple individual particles with the same physical and kinetic properties. The number of real particles that constitutes a computational parcel is quantified using a scaling factor called the super particle loading, α^2, whose value is set based on the volume/mass fraction of the particles and computational memory available. For particle–gas systems, the reported α^2 in previous literature ranges from $O(10^1)$ to $O(10^3)$ (Osnes *et al.* 2017; Koneru *et al.* 2020; Xue *et al.* 2020). In the present work, α^2 is of $O(10^1)$.

For the gas phase, the volume-averaged governing equations (2.1)–(2.3) constructed in the Eulerian frame are based on a five-equation transport model, i.e. a simplified form of the Baer–Nunziato model (Baer & Nunziato 1986); this model has been modified to account for compressible multiphase flows ranging from dilute to dense gas–particle flows (Carmouze *et al.* 2020; Chiapolino & Saurel 2020).

$$\frac{\partial(\varepsilon\rho_f)}{\partial t} + \nabla \cdot (\varepsilon\rho_f \boldsymbol{u}_f) = 0, \tag{2.1}$$

$$\frac{\partial(\varepsilon\rho_f \boldsymbol{u}_f)}{\partial t} + \nabla \cdot (\varepsilon\rho_f \boldsymbol{u}_f \boldsymbol{u}_f) + \nabla(\varepsilon P_f) = P_f \nabla\varepsilon + \sum_i [\phi_{p,i}\rho_{p,i}D_{p,i}(\boldsymbol{u}_{p,i} - \bar{\boldsymbol{u}}_f)], \tag{2.2}$$

$$\frac{\partial(\varepsilon\rho_f E_f)}{\partial t} + \nabla \cdot (\varepsilon\rho_f E_f \boldsymbol{u}_f + \varepsilon P_f \boldsymbol{u}_f) = P_f \nabla\varepsilon \cdot \bar{\boldsymbol{u}}_p + \sum_i [\phi_{p,i}\rho_{p,i}D_{p,i}(\boldsymbol{u}_{p,i} - \bar{\boldsymbol{u}}_f) \cdot \boldsymbol{u}_{p,i}]. \tag{2.3}$$

The volume fraction of gas phase, i.e. porosity, is expressed by ε. The volume fraction of particle phase is expressed by ϕ_p, while $\varepsilon + \phi_p = 1$ in the same fluid grid. The velocity, density, pressure and total energy of the gas are represented by $\boldsymbol{u}_f$, ρ_f, P_f and E_f, respectively. Here $E_f = e_f + 0.5\boldsymbol{u}_f\boldsymbol{u}_f$, where e_f is the specific internal energy. Terms $\phi_{p,i}$, $\rho_{p,i}$, $D_{p,i}$ and $\boldsymbol{u}_{p,i}$ are local volume fraction, density, drag force coefficient and velocity of parcel i. Parameter $\bar{\boldsymbol{u}}_f$ represents the average fluid velocity at the location of particle i and $\bar{\boldsymbol{u}}_p$ represents the average velocity of particles within a fluid cell. Notably, the first term on the right-hand side of (2.2), $P_f \nabla\varepsilon$, is the nozzling term that becomes significant wherever the porosity gradient is non-trivial.

We employ the Di Felice model combined with Ergun's equation to calculate D_p, which is essentially a nonlinear drag force model (Di Felice 1994). The Di Felice model combined with Ergun's equation (Ergun 1952) considers the effects of both the particle Reynolds number, Re_p, and the porosity, ε, and has been widely used in particle-laden multiphase flows (Kafui, Thornton & Adams 2002; Feng *et al.* 2004). Parameter D_p is a function of Re_p and ε:

$$D_{p,i} = \frac{3}{8sg}C_d\frac{|\bar{\boldsymbol{u}}_f - \boldsymbol{u}_{p,i}|}{r_p}, \tag{2.4}$$

$$C_d = \frac{24}{Re_p}\begin{cases} 8.33\dfrac{1-\varepsilon}{\varepsilon} + 0.0972Re_p & \text{if } \varepsilon < 0.8, \\ f_{base} \cdot \varepsilon^{-\zeta} & \text{if } \varepsilon \geq 0.8, \end{cases} \tag{2.5}$$

$$f_{base} = \begin{cases} 1 + 0.167Re_p^{0.687} & \text{if } Re_p < 1000, \\ 0.0183Re_p & \text{if } Re_p \geq 1000, \end{cases} \tag{2.6}$$

$$\zeta = 3.7 - 0.65\exp[-\tfrac{1}{2}(1.5 - \log_{10}Re_p)^2], \tag{2.7}$$

where C_d is the dimensionless coefficient of the drag force, sg is the specific weight of individual particles, $sg = \rho_p/\rho_f$, and r_p is the particle radius. For dense particle flows ($\varepsilon < 0.8$), (2.4) reduces to the original Ergun equation. Otherwise, C_d takes the form of the Stokes law multiplied by a correction coefficient which varies with Re_p, as indicated by (2.6) and (2.7).

The particle phase is represented by discrete parcels whose motion is governed by Newton's second law ((2.8) and (2.9)):

$$\frac{\mathrm{d}\boldsymbol{u}_{p,i}}{\mathrm{d}t} = D_{p,i}(\bar{\boldsymbol{u}}_f - \boldsymbol{u}_{p,i}) - \frac{1}{\rho_p}\boldsymbol{\nabla}\langle P_f \rangle + \frac{1}{m_p}\sum_j \boldsymbol{F}_{C,ij}, \tag{2.8}$$

$$\frac{\mathrm{d}\boldsymbol{x}_{p,i}}{\mathrm{d}t} = \boldsymbol{u}_{p,i}, \tag{2.9}$$

where $\boldsymbol{x}_{p,i}$ and $\boldsymbol{m}_{p,i}$ denote the displacement and mass of parcel i, respectively, and $\boldsymbol{F}_{C,ij}$ represents the collision force between parcels i and j.

A four-way coupling strategy (Ukai *et al.* 2010) was adopted to account for the momentum and energy transfer between the gases and particles. Specifically, the drag force and the associated work from particles were incorporated into the momentum (2.2) and energy (2.3) equations of the gas phase as the source terms. The parcels are driven by the pressure gradient force, drag force and collision force between themselves (equation (2.8)). A soft sphere model, represented by a coupling spring and dashpot, was employed to model the collision force between the parcels (Apte, Mahesh & Lundgren 2003). Hence, $\boldsymbol{F}_{C,ij}$ consists of a repulsive force and a damping force, as follows:

$$\boldsymbol{F}_{C,ij} = k_{n,p}\boldsymbol{\delta}_n - \gamma_{n,p}\boldsymbol{u}_{n,ij}, \tag{2.10}$$

where $k_{n,p}$ and $\gamma_{n,p}$ are the stiffness and damping coefficients of the parcels, respectively, and δ_n and $\boldsymbol{u}_{n,ij}$ are the overlap and normal velocity difference between parcels in contact, respectively. Here $\gamma_{n,p}$ is a function of the parcel restitution coefficient e_p (Crowe *et al.* 2012) and defined as follows:

$$\gamma_{n,p} = -\frac{2\ln e_p}{\sqrt{\pi^2 + \ln e_p}}\sqrt{m_p k_{n,p}}. \tag{2.11}$$

To solve the equations governing the gases, the weighted essentially non-oscillatory (Liu *et al.* 1994) scheme was used to reconstruct the primary flow variables. A Riemann solver proposed by Harten, Lax and van Leer (Toro 2013) was used to obtain the intercell fluxes. The third-order Runge–Kutta method was applied for the time integration. The equations describing the parcel velocity and position were discretized by the velocity-Verlet algorithm (Kruggel-Emden *et al.* 2008). Bilinear/trilinear interpolation functions were adopted to calculate the particle volume fraction and source terms on the Eulerian grids, as well as the fluid variables on the Lagrangian parcels. Numerical details with regard to CMP-PIC can be found in our previous studies (Meng *et al.* 2019; Tian *et al.* 2020; Xue *et al.* 2020; Li *et al.* 2021).

The present CMP-PIC framework has been validated against Rogue's experiments involving shock waves propagating through particle curtains (Tian *et al.* 2020), shock tube experiments wherein particle columns are impinged head-on by incident shocks (Tian *et al.* 2020) and shock dispersion of particle rings (Xue *et al.* 2020). Specifically, CMP-PIC reproduces the pore pressure histories at the cross-sections along the length of the granular columns with different distances from the front surface, and its results are

in good agreement with the experimentally recorded pressure traces. These validations ensure that the CMP-PIC capacity can adequately simulate the evolution of the mean flow parameters during shock-induced gas filtration.

2.2. *The Morrison approach*

The Morrison approach consisting of a simplified momentum conservation equation enables the investigation of the dynamics of the mean flow parameters in shock-induced gas filtration under the isothermal assumption. The results serve as a comparison with the CMP-PIC simulated results to determine the influences of the thermal effects on the mean flow parameters. Prior to presenting the non-dimensional equation for the pressure rise along the granular column developed by Morrison (Morrison 1972), two non-dimensional parameters that play deciding roles in gas filtration were introduced (Britan *et al.* 2007). The first is the effective Reynolds number, Re_f, whose formulation is shown as follows:

$$Re_f = \frac{P_5 - P_1}{P_1} \cdot \frac{b}{a^2} \cdot \frac{1}{l} \cdot \frac{c_1^2}{v_1^2 \gamma}, \tag{2.12}$$

where P_5 and P_1 are the upstream and downstream pressure upon the shock reflection off the front surface of porous column, respectively, l is the length of porous column, c_1 is the sound speed, $c_1 = (\gamma P_1/\rho_1)^{1/2}$, v_1 is the kinematic viscosity, $v_1 = \mu_1/\rho_1$, γ is the specific ratio and a and b are the Darcy and Forchheimer coefficients mentioned above with (1.1). Note that the subscript 1 in (2.12) and hereafter refers to the parameters of the quiescent air ahead of the incident shock wave. The second parameter is the non-dimensional intensity of the pressure impact that is imposed by the shock wave reflected at the front edge of a granular sample, N, as follows:

$$N = \frac{P_5 - P_1}{P_1}. \tag{2.13}$$

The upstream pressure, P_5, is a function of M_s given by the normal shock relation:

$$P_5 = \frac{(7M_s^2 - 1)(4M_s^2 - 1)}{3(M_s^2 + 5)} P_1. \tag{2.14}$$

Therefore, N is also a function of M_s. If the quiescent air ahead of the incident shock wave is under ambient conditions with $P_1 = 101.325$ kPa and $T_1 = 298.15$ K and has a specific heat ratio for ideal gases of 1.4, then substituting (2.14) into (2.13) we obtain the following:

$$N = \frac{(7M_s^2 - 1)(4M_s^2 - 1)}{3(M_s^2 + 5)} - 1. \tag{2.15}$$

Comparing the formulations of Re_f and N, Re_f evidently comprises N, and the remnant constituting a third non-dimensional parameter is denoted as Π, as follows:

$$\Pi = \frac{b}{a^2} \cdot \frac{1}{l} \cdot \frac{c_1^2}{v_1^2 \gamma}. \tag{2.16}$$

For a granular medium composed of spherical granules, the Darcy and Forchheimer coefficients, a and b, are functions of only the particle diameter, d_p, and the granular

medium porosity, ε, through Ergun's relations, as follows:

$$a = 180\frac{(1-\varepsilon)^2}{\varepsilon^2}\frac{1}{d_p^2}, \quad b = 1.8\frac{1-\varepsilon}{\varepsilon}\frac{1}{d_p}. \tag{2.17a,b}$$

Substituting (2.17) into (2.16) leads to the following:

$$\Pi = \left(\frac{1.75}{150^2}\cdot\frac{\rho_1 P_1}{\mu_1^2}\right)\cdot\left[\frac{1}{l}\frac{(1-\phi_p)^3}{\phi_p^3}d_p^3\right]. \tag{2.18}$$

As evident from (2.18), Π incorporates the properties of the quiescent gases inside and downstream of the granular column prior to shock impingement as well as the structural properties of the granular column. Notably, the CMP-PIC and Morrison models both employ Ergun's equation to account for the drag force between the solid skeleton and the interstitial gases.

In line with Morrison's derivation, the scaling factor for the length is the length of the granular column, while the scaling factor for the time, t_{sc}, is given by the following:

$$t_{sc} = l^2 a\frac{\gamma\nu_1}{c_1^2 N} = l^2 a\frac{\mu_1}{P_1 N}. \tag{2.19}$$

Therefore, the scaling factor for the velocity is $V_{sc} = l/t_{sc}$. The non-dimensional variables for the distance, χ, and the time, τ, the pressure, θ, and the velocity, V^*, are as follows:

$$\chi = \frac{x}{l}, \quad \tau = \frac{t}{t_{sc}}, \quad \theta = \frac{P_f - P_1}{P_5 - P_1}, \quad V^* = \frac{u_f}{V_{sc}} = \frac{alu_f\mu_1}{P_5 - P_1}. \tag{2.20a–d}$$

As a consequence, the non-dimensional form of the Forchheimer resistance law becomes the following:

$$\frac{\partial\theta}{\partial\chi} = -V^* - Re_f(1+N\theta)V^*|V^*|. \tag{2.21}$$

The mass conservation equation becomes the following:

$$N\frac{\partial\theta}{\partial\tau} + \frac{\partial}{\partial\chi}[V^*(1+N\theta)] = 0. \tag{2.22}$$

Combining (2.21) and (2.22) results in the following:

$$\frac{\partial\theta}{\partial\tau} = \frac{1}{\sqrt{1 + 4Re_f(1+N\theta)\left|\dfrac{\partial\theta}{\partial\chi}\right|}}\left[\left(\frac{1}{N}+\theta\right)\frac{\partial^2\theta}{\partial\chi^2} + \left(\frac{\partial\theta}{\partial\chi}\right)^2\right]. \tag{2.23}$$

Equation (2.23) describes the filtration flows complying with the so-called mixed conditions, i.e. flows in which both the viscous and the inertial losses are dominant. The numerical solution of (2.23) provides the transient pressure profiles along a granular column under the isothermal assumption.
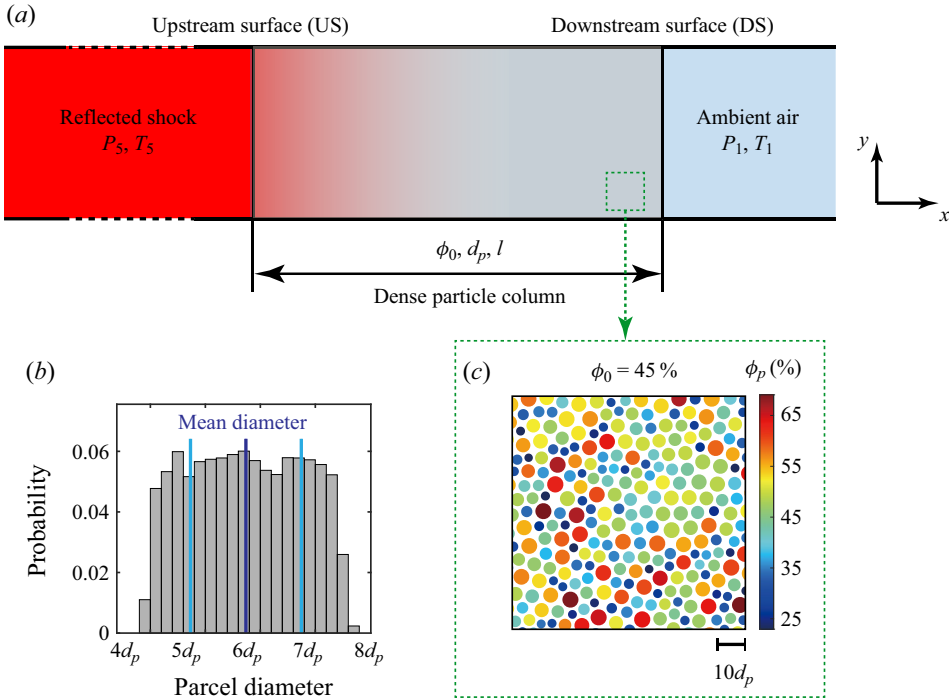
(a)

(b)

(c)

Figure 2. (a) Schematic diagram of the shock-tube-based configuration in the numerical experiments. (b) Histogram of the parcel diameter distribution. (c) Close-up image of initial particle packing coloured by the local particle volume fraction for the case with $\phi_0 = 45 \%$.

3. Numerical set-up

A two-dimensional configuration illustrated in figure 2(a) was employed to investigate shock-induced gas filtration in densely packed granular columns with rigid solid skeletons. Instead of simulating the impingement of an incident shock upon the front surface of the granular column, the state of the gases upstream of the front surface is kept as that compressed by the reflected shock arising from the reflection of the incident shock off the rigid surface. Hence, the upstream pressure and temperature are kept constant, consistent with the reflected pressure, P_5, and temperature, T_5, given by (2.14) and (3.1), respectively:

$$T_5 = \frac{(4M_s^2 - 1)(M_s^2 + 2)}{9M_s^2} T_1. \tag{3.1}$$

In this way we reduce the unsteady reflection process characterized by the coalescence of a major reflected shock and a number of trailing compression waves to an instantaneous reflection so that any disturbances associated with the unsteady reflection are eliminated. The intergrain pores and downstream regions are filled with ambient air at $P_1 = 1.0 \times 10^5$ Pa and $T_1 = 298$ K.

The granular column domain was filled by particles generated by the radius expansion algorithm. A population of parcels with artificially small radii that ensure that no parcel or wall overlap is first randomly created within the specified volume. Then, all parcels are expanded until the specified particle size distribution and desired porosity are satisfied (Yan *et al.* 2009). In the present work, the diameter of the real particle is d_p, while the diameter of the parcel uniformly ranges from $4d_p$ to $7.5d_p$ μm to avoid
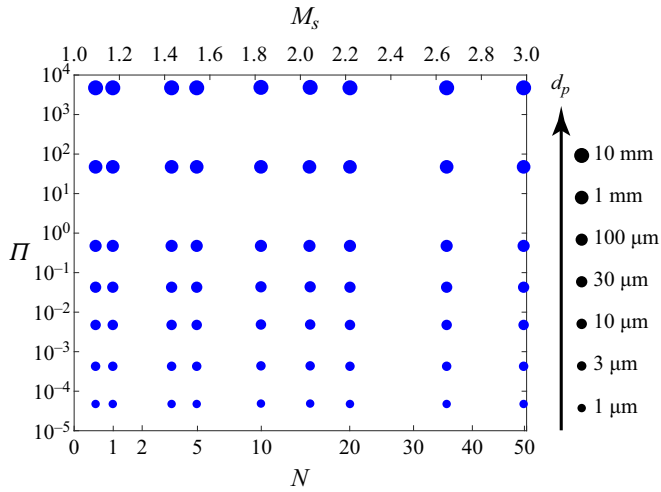
Figure 3. Distribution of the simulated systems in the non-dimensional parametric space (N, Π). The symbol size varies according to the diameter of spherical particles d_p.

potential crystallization during shock compaction (see the histogram of the parcel diameter distribution in figure 2*b*). The close-up image in figure 2(*c*) shows the particle packing with $\phi_0 = 45\,\%$ wherein the parcels are coloured by the parcel-scale particle volume fraction, ϕ_p, calculated using Voronoi tessellation. A random but homogeneous arrangement of parcels is achieved regardless of the overall volume fraction.

In this study, the aim is to elucidate the thermal effect in shock-induced gas filtration, which has universal implications. Hence, we constructed a comprehensive set of systems with distinctively varying combinations of two deciding non-dimensional parameters of N and Π. Figure 3 shows the largely even distribution of dozens of simulated systems in the non-dimensional parametric space (N, Π). Since Π is a function of M_s, systems can be readily distinguished from each other by the combination of M_s and Π as shown in figure 3. For clarity, the system is labelled by values of M_s and Π, C-M_s-Π.

As the incident shock intensifies, N increases from zero to 50 as M_s increases from 1 to 3 while the non-dimensional upstream temperature, $T_5^* = T_5/T_1$, increases almost five times, as indicated in figures 4(*a*) and 4(*b*), respectively. For an incident shock with $M_s = 3$, T_5 is elevated as high as 1406 K, indicating a considerable temperature difference between the upstream and the downstream.

Compared with the relatively modest variation in N, the values of Π span nine orders of magnitude, varying from $O(10^{-5})$ to $O(10^4)$. To achieve this drastically wide variation range of Π, the primary affecting variable, d_p, was allowed to vary between $O(10^{-6})$ and $O(10^{-2})$ m, as shown in figure 3. Another two variables, l and ϕ_0, vary within relatively narrow ranges, $l \sim 200d_p$–$1000d_p$, $\phi_0 \sim 0.45$ to 0.6, entailing densely packed and long granular columns. Low porosities are needed by the approximation of the shock reflection off the solid surface. The long column ensures that the variation length of the mean flows is greater than the particle size. The values of ϕ_0 presented here are those in the equivalent three-dimensional assemblies converted from the porosity correlation between the two- and three-dimensional packings proposed by Borchardt-Ott (2012):

$$\varepsilon_{3D} = 0.2595 + \frac{\varepsilon_{2D} - 0.0931}{0.2146 - 0.0931}(0.4760 - 0.2595). \tag{3.2}$$
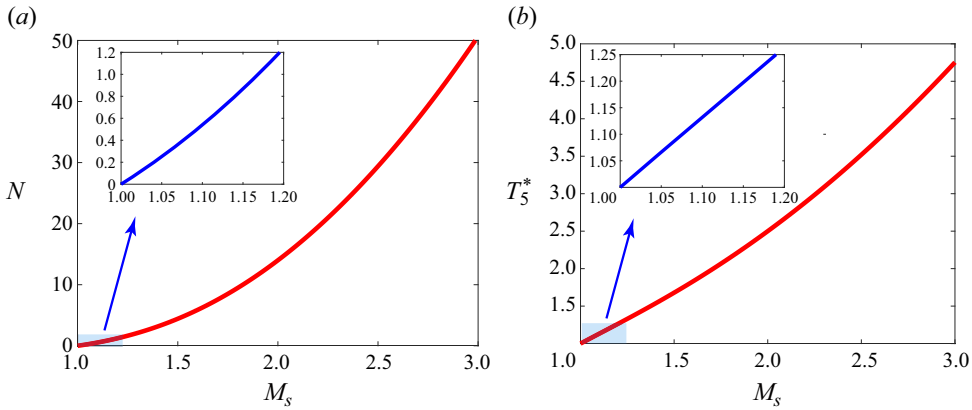
(*a*)

(*b*)

Figure 4. Variations in N (*a*) and T_5^* (*b*) with the Mach number of the incident shock, M_s. Insets: close-up images for part of the $N(M_s)$ and $T_5^*(M_s)$ curves towards the lower limiting end ($M_s < 1.2$).

The values in (3.2), 0.2595 (0.4760) and 0.0931 (0.2146), are associated with the states of maximum or minimum packing density in two-dimensional (three-dimensional) packings composed of monodispersed spheres. This conversion correlation has been widely used to convert ϕ_{2D} to ϕ_{3D}, and *vice versa*. Accordingly, three-dimensional particle volume fractions, ϕ_{3D}, from 0.45 to 0.6 correspond to two-dimensional particle volume fractions, ϕ_{2D}, from 0.75 to 0.83. The exact values of the variable parameters in each numerical case are listed in table 1 in Appendix A.

4. Results and analysis

4.1. *Pressure diffusion*

Figure 5(*a*) shows the typical profiles of non-dimensional pressure fields in C-1.43-50 as a function of depth into the granular column, $\theta_{iso}(\chi)$ and $\theta_{non\text{-}iso}(\chi)$, at different times. The variables with the subscripts '*iso*' and '*non-iso*' represent the results derived from the Morrison model with the isothermal assumption and the CMP-PIC simulations that assume non-isothermal processes, respectively. These variables are referred to as either the isothermal or the non-isothermal results hereafter. Note that the profiles $\theta_{non\text{-}iso}(\chi)$ are calculated as the average pressure across the width of the granular column (perpendicular to the flow direction). The same averaging method is applied to derive the streamwise profile of other flow and thermodynamic parameters, such as the profiles of gas velocity, temperature and density. Despite the universal decay characteristics of the diffusing pressure fields, the profiles $\theta_{non\text{-}iso}(\chi)$ are always above the profile $\theta_{iso}(\chi)$ until a steady diffusing pressure field is established. The coincidence of the converged profiles $\theta_{non\text{-}iso}(\chi)$ and $\theta_{iso}(\chi)$ indicates that the steady pressure diffusing field is unaffected by the nature (isothermal or non-isothermal) of the prior unsteady phase.

To qualitatively compare the two pressure diffusion processes, we look at the evolution of a characteristic depth χ_s of the pressure field with time, where χ_s is the depth into the medium with a decayed pressure profile of $\theta(\chi_s) = 0.01$, as illustrated in the inset of figure 5(*a*). As shown in figure 5(*b*), the $\chi_{s,non\text{-}iso}(\tau)$ trajectory precedes the $\chi_{s,iso}(\tau)$ trajectory from the very beginning, indicating markedly faster pressure diffusion during the non-isothermal filtration. If the characteristic time of the pressure diffusion, τ_{diff}, is measured by the time upon which χ_s reaches the rear surface of the granular column,
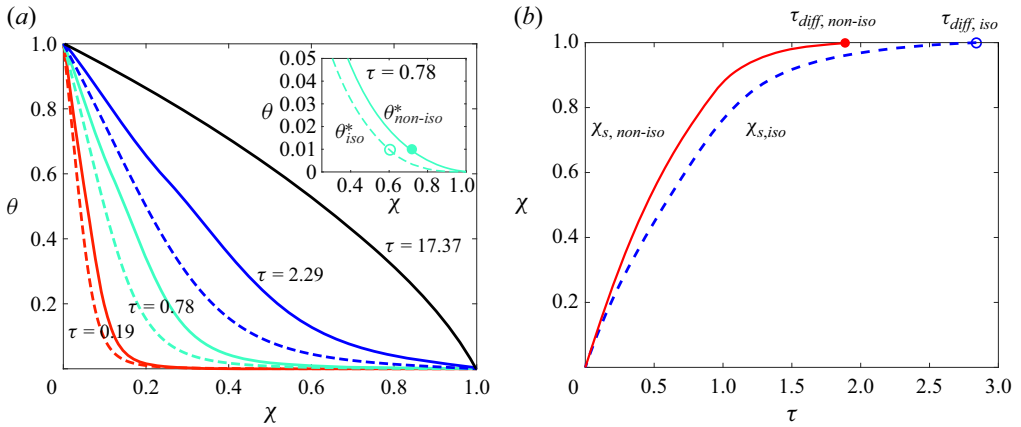
999 A91-11

Figure 5. (*a*) Profiles of the isothermal (dashed line) and non-isothermal (solid line) pressure fields, $\theta_{iso}(\chi)$ and $\theta_{non\text{-}iso}(\chi)$, for C-1.43-50 during the unsteady and steady filtration phases. Unsteady phase: $\tau = 0.19$, 0.78 and 2.29; steady phase: $\tau = 17.37$. Note that the steady $\theta_{iso}(\chi)$ and $\theta_{non\text{-}iso}(\chi)$ profiles converge into an identical profile. Inset: zoomed-in details of $\theta_{iso}(\chi)$ and $\theta_{non\text{-}iso}(\chi)$ at $\tau = 0.78$ with markers indicating the characteristic depth of the isothermal and non-isothermal pressure diffusion, $\chi_{s,iso}$ and $\chi_{s,non\text{-}iso}$. (*b*) Trajectories of $\chi_{s,iso}(\tau)$ and $\chi_{s,non\text{-}iso}(\tau)$ for C-1.43-50.

$\chi_s = 1$, the isothermal pressure diffusion in C-1.43-0.5 is almost 50 % slower than its non-isothermal counterpart since $\tau_{diff,iso} = 2.84$ while $\tau_{diff,non\text{-}iso} = 1.9$.

The heat influx carried by the high-temperature upstream gases contributes to the expediting of unsteady pressure diffusion due to additional energy input. The expediting of the non-isothermal pressure diffusion compared with its isothermal counterpart is quantified by the characteristic time ratio between isothermal and non-isothermal pressure diffusions, $\xi_p = \tau_{diff,iso}/\tau_{diff,non\text{-}iso}$. Figure 6(*a*) plots ξ_p for all systems using symbols whose size and colour vary with the values of the respective ξ_p. By interpolating ξ_p in figure 6(*a*), the contour map of ξ_p is rendered in the parameter space (M_s, Π) as shown in figure 6(*b*). In general, ξ_p increases with either M_s or Π resulting in the isolines slanting from the upper left to the lower right. However, the increasing rates markedly vary from region to region as the isolines of ξ_p become increasingly steeper with M_s and Π approaching the upper limit. The varying expediting effect in the parameter space (M_s, Π), as a manifestation of the thermal effect, is further discussed in § 4.4.

Notably, the non-isothermal and isothermal pressure diffusion are comparable inside the bottom left semi-triangular region delimitated by the isoline $\xi_p = 1.1$; therefore, the isothermal assumption holds therein in terms of the pressure diffusion. Hence, this triangular region is referred to as the pressure diffusion equivalent triangle denoted by TR_{diff}. The upper boundary of TR_{diff}, namely isoline $\xi_p = 1.1$, can be well fitted by the linear correlation between M_s and Π, as follows:

$$M_s = -0.6 \lg \Pi + 0.22. \tag{4.1}$$

In addition to the expedited unsteady diffusion phase, the non-isothermal pressure diffusion also exhibits distinct behaviours between $\tau_{diff,non\text{-}iso}$ and the full development of the steady pressure field. Figure 7 depicts the temporospatial evolutions of the thermal and non-isothermal diffusing pressure fields for C-1.43-50 represented by the isolines $\theta_{iso}(\chi,\tau)$ and $\theta_{non\text{-}iso}(\chi,\tau)$, respectively. In contrast to the monotonic convergence of the isolines $\theta_{iso}(\chi,\tau)$, the majority of isolines $\theta_{non\text{-}iso}(\chi,\tau)$ undergo discernible retraction after $\chi_{s,non\text{-}iso}$ reaches the rear surface of the granular column. The retraction starts at the rear
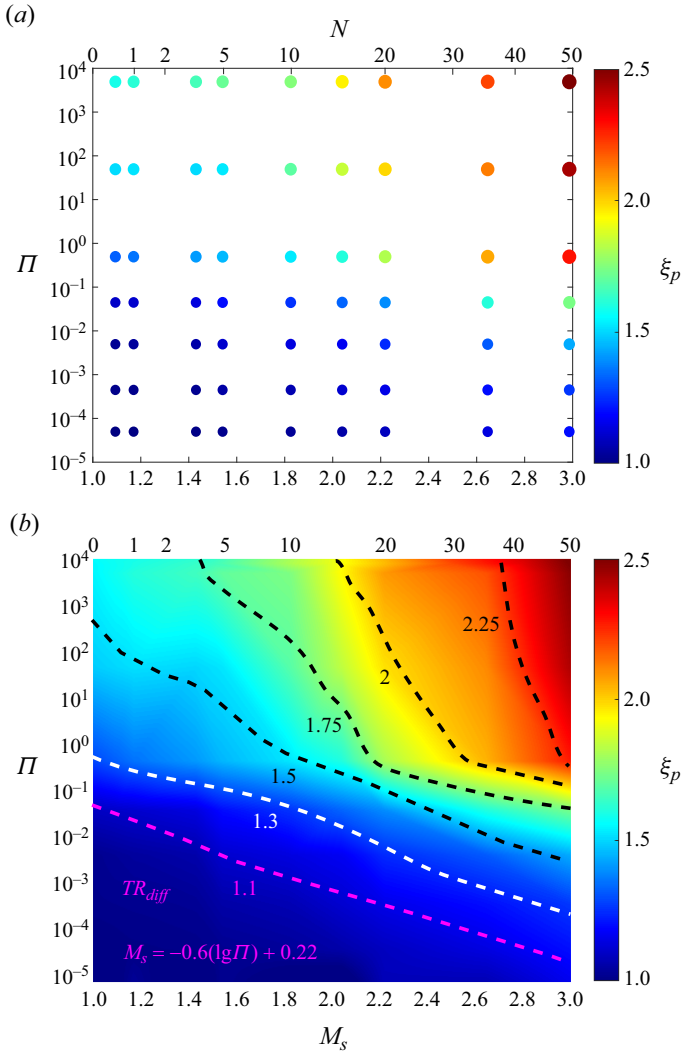
999 A91-12

Figure 6. (*a*) Characteristic time ratio between isothermal and non-isothermal pressure diffusions, ξ_p, for all simulated systems represented by filled circles whose size and colour vary with the values of the respective ξ_p. (*b*) Contour map of ξ_p in the parameter space (M_s, Π) rendered by interpolating the data in (*a*). Isolines of ξ_p are superimposed in (*b*). Note that the isoline ξ_p, $\xi_p = 1.1$, which can be approximated by the linear function given in (4.1), sets the upper boundary of TR_{diff}.

surface and propagates upstream with a decaying retraction extent. As discussed in § 4.2, the retraction of $\theta_{non\text{-}iso}(\chi, \tau)$ is associated with the flow acceleration at the immediate neighbourhood of the rear surface due to the nozzling effect which is amplified in the non-isothermal gas filtration.

4.2. *Gas flows*

Figure 8 shows the profiles of isothermal and non-isothermal gas velocity fields in C-1.43-50 as a function of depth into the granular column, $V_{iso}^*(\chi)$ and $V_{non\text{-}iso}^*(\chi)$, at times corresponding to figure 5. In contrast with the decaying profiles $\theta_{iso}(\chi)$ and $\theta_{non\text{-}iso}(\chi)$, the
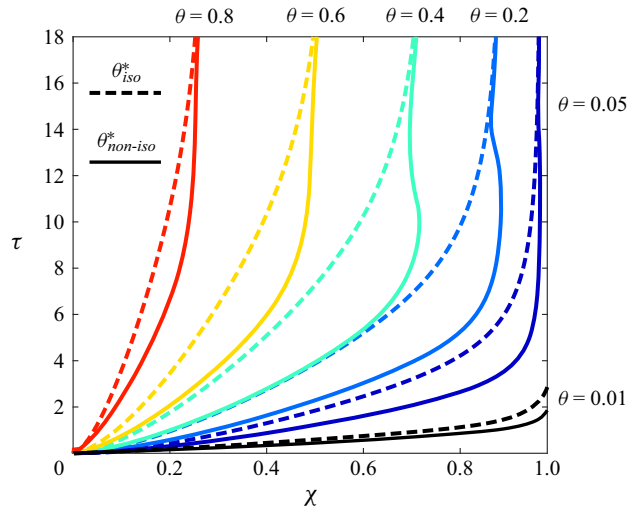
Figure 7. Temporospatial evolutions of the isothermal and non-isothermal diffusing pressure fields in C-1.43-50. Dashed and solid curves represent the isolines of $\theta_{iso}(\chi, \tau)$ and $\theta_{non\text{-}iso}(\chi, \tau)$, respectively.

profiles $V^*_{iso}(\chi)$ and $V^*_{non\text{-}iso}(\chi)$ both exhibit non-monotonic characteristics with singular velocity peaks formed at the very beginning of gas filtration. As the profiles $V^*_{iso}(\chi)$ and $V^*_{non\text{-}iso}(\chi)$ extend downstream with time, the downstream-moving velocity peak quickly flattens. After $\chi_{s,iso}$ (and $\chi_{s,non\text{-}iso}$) reaches the rear surface, a rear tail emerges and lifts up with time, indicating that the flows accelerate towards the rear surface. This phenomenon of flow acceleration is widely observed and attributed to the rapid fluid volume fraction changes across the rear surface, since the momentum and energy changes of the filtration flow due to the nozzling term (in (2.2) and (2.3)) become significant (Bdzil *et al.* 1999; Kalenko & Liberzon 2020; Choi & Park 2022). Therefore, we describe the increase of fluid velocity caused by changes in volume fraction as the 'nozzling effect' in this paper. The rear-surface region across which the flows increasingly accelerate is denoted as RSR_{acc}.

For isothermal gas filtration, the correlation between the gas pressure and velocity is described by the Forchheimer resistance law (2.21). In the Darcy-flow domain, the Forchheimer resistance law reduces to the Darcy resistance law whereby the instantaneous gas velocity is proportional to the local pressure gradient. The velocity gradient depends on the quadratic differential of the pressure. Hence the profile $V^*_{iso}(\chi)$ peaks at the deflection point of the pressure gradient curve, $\partial_\chi \theta_{iso}(\chi)$, upon which $\partial_\chi V^*_{iso}(\chi)$ and $\partial^2_\chi \theta^*_{iso}$ are zero. Similarly, the signature peak in the profile $V^*_{non\text{-}iso}(\chi)$ also arises from the deflection of $\partial_\chi \theta_{non\text{-}iso}(\chi)$. Indeed, the deflection points in profiles $\partial_\chi \theta_{iso}(\chi)$ and $\partial_\chi \theta_{non\text{-}iso}(\chi)$ shown in figure 8(*b*) coincide with the locations of the peak summits of profiles $V^*_{iso}(\chi)$ and $V^*_{non\text{-}iso}(\chi)$, respectively.

The temporospatial evolutions of the non-isothermal and isothermal gas velocity fields for C-1.43-50 plotted in figure 9(*a,b*) show similar patterns. However, the non-isothermal gas flows are considerably faster than the isothermal flows. Notably, the rear-surface acceleration for the non-isothermal filtration is much more evident and affects the regions far removed from the rear surface. Accordingly, the rarefaction waves accompanying the development of the rear-surface accelerating flows are stronger in the non-isothermal filtration, sufficing to cause the marked retraction of $\theta_{non\text{-}iso}(\chi, \tau)$ contour lines in figure 7.

For compressible gas flows, the velocity fields are closely coupled with the thermodynamic parameters. Thus, to gain a thorough understanding of the thermodynamic
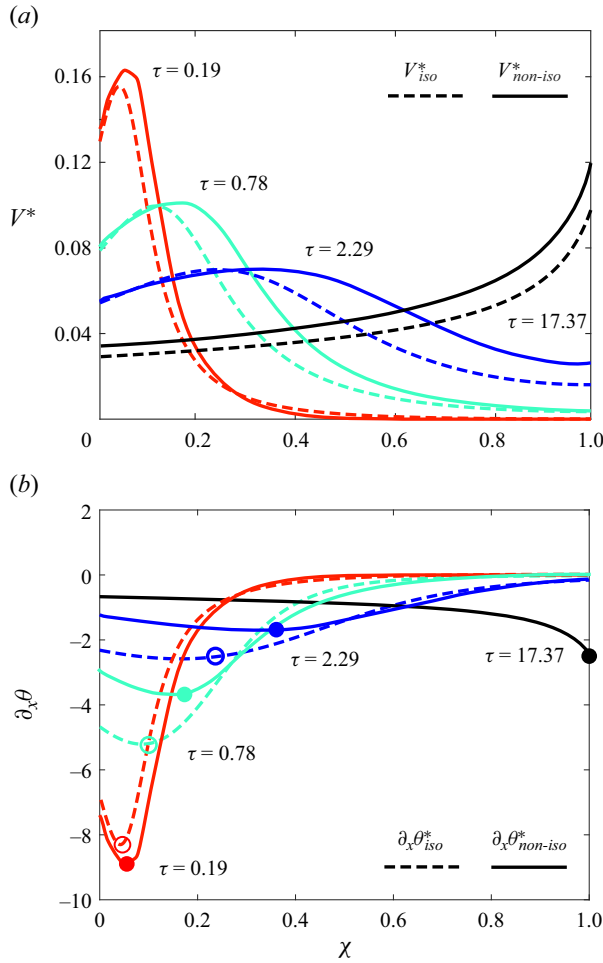
999 A91-14

Figure 8. (*a*) Typical profiles of $V_{iso}^*(\chi)$ (dashed line) and $V_{non-iso}^*(\chi)$ (solid line) for C-1.43-50 during the unsteady and steady filtration phases. Unsteady phase: $\tau = 0.19$, 0.78 and 2.29; steady phase: $\tau = 17.37$. (*b*) Corresponding pressure gradient profiles, $\partial_\chi \theta_{iso}(\chi)$ and $\partial_\chi \theta_{non-iso}(\chi)$, with markers indicating the locations of the velocity peaks.

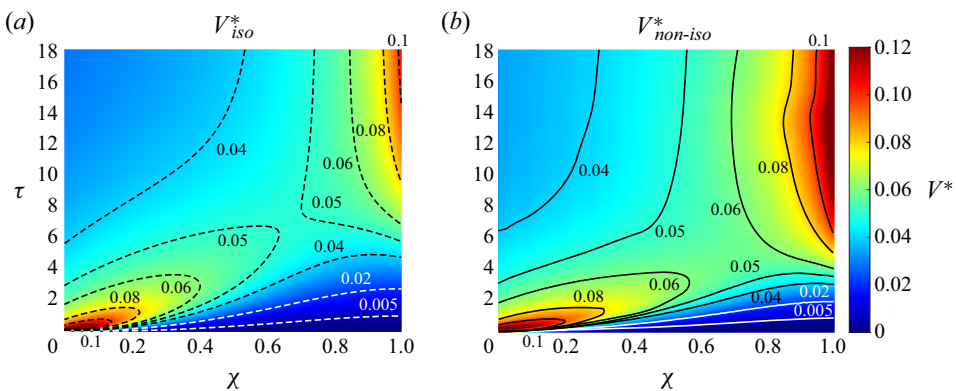Figure 9. Temporospatial evolutions of $V_{iso}^*(\chi, \tau)$ (*a*) and $V_{non-iso}^*(\chi, \tau)$ (*b*) for C-1.43-50 superimposed with the velocity isolines.
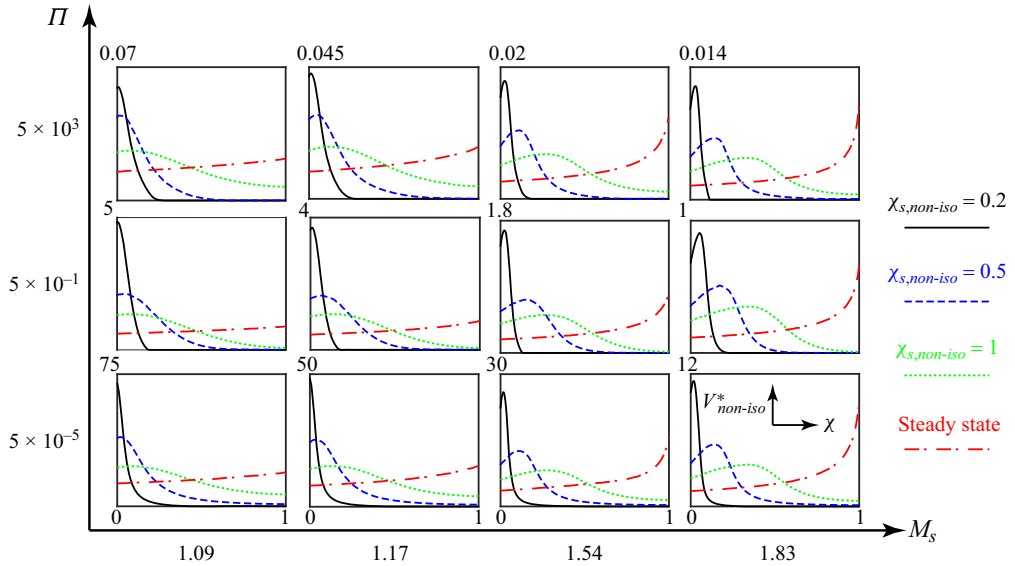
Figure 10. Successions of profiles $V^*_{non\text{-}iso}(\chi)$ for a range of systems with varying M_s and Π, displaying a complete evolution of velocity fields. The $\chi_{s,non\text{-}iso}$ values corresponding to the first three profiles $V^*_{non\text{-}iso}(\chi)$ from left to right are 0.2, 0.5 and 1, represented by the solid black, the dashed blue and the dotted green lines, respectively. The fourth profile in the dashed-dotted red line represents the steady flow.

parameters in the non-isothermal gas filtration, the evolving flow characteristics need to be elucidated. Figure 10 shows the velocity profiles $V^*_{non\text{-}iso}(\chi)$ for a range of systems with M_s and Π spanning the entire parameter space. The first three profiles from left to right describe the streamwise velocity distributions at the moments of the filtration incipiency ($\chi_{s,non\text{-}iso} = 0.2$), the half-column being infiltrated ($\chi_{s,non\text{-}iso} = 0.5$) and the flows reaching the rear surface ($\chi_{s,non\text{-}iso} = 1$). The fourth profile is the converged profile corresponding to the steady pressure diffusion phase.

Although the progression of $V^*_{non\text{-}iso}(\chi)$ displayed in figure 10 exhibits a similar trend to that shown in figure 9(a), the influences from M_s and Π cause distinct flow characteristics, from very incipient unsteady flows to well-developed steady flow. As M_s increases the primary velocity peak in the incipient $V^*_{non\text{-}iso}(\chi)$ becomes increasingly prominent with an elevated amplitude and steepened declining slope. The peak amplitude is quantified by $\Delta V^*_{peak} = (V^*_{peak} - V^*_0)/V^*_0$, where V^*_{peak} and V^*_0 represent the peak velocity and velocity at the front surface, respectively. Figure 11 shows the dependence of ΔV^*_{peak} on M_s with $\Pi = 5 \times 10^{-5}$, 0.5 and 5×10^4. Here, ΔV^*_{peak} is calculated based on the profile $V^*_{non\text{-}iso}(\chi)$ with $\chi_{s,iso} = 0.5$. The M_s dependence of ΔV^*_{peak} demonstrates an asymptotic convergence trend regardless of Π varying over nine orders of magnitude, while ΔV^*_{peak} is negligible ($\Delta V^*_{peak} < 0.05$) in the weakest shock domain ($M_s < 1.1$).

Another striking flow characteristic associated with the increased M_s is the amplified tail rising of the velocity profile, indicating an enhanced rear-surface acceleration. Figure 12(a) shows a comparison of the profiles $V^*_{non\text{-}iso}(\chi)$ for the steady flows in systems with $\Pi = 0.5$ and increasing M_s; significant steepening and narrowing of the lifting tails are observed. Except for the lifting tail, the bulk of the velocity profiles can be effectively fitted by a linear function as indicated in figure 12(a). Thus, the point beyond which the extrapolated fitting line and the actual profile become non-trivial is considered to be the beginning
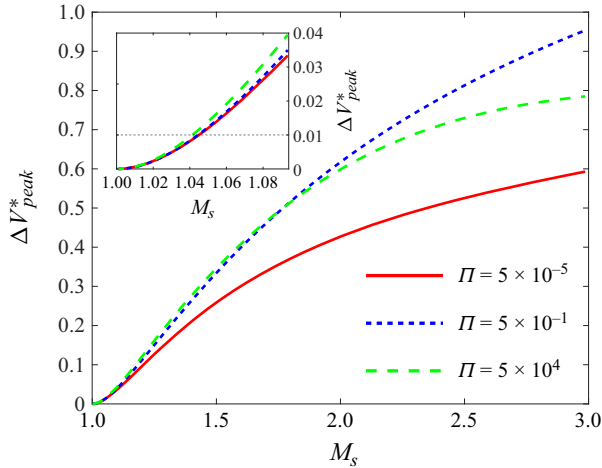
999 A91-16

Figure 11. Variations in ΔV^*_{peak} with M_s. Inset: zoom-in plot of $\Delta V^*_{peak}(M_s)$ in the weakest incident shock domain, $M_s < 1.1$.
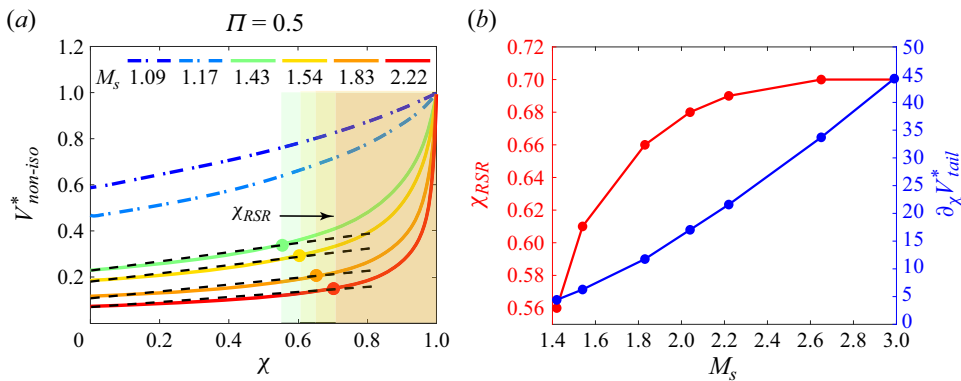

Figure 12. (*a*) Comparison of the profiles $V^*_{non\text{-}iso}(\chi)$ for the steady flows in systems with increasing M_s; the circle symbols indicate the front edges of the RSR_{acc} beyond which the linear fitted lines denoted by the dashed line start to deviate from the actual profiles. (*b*) The M_s dependence of the front edge of the RSR_{acc}, χ_{RSR} (left axis), and the tail rising rate, $\partial_\chi V^*_{tail}$ (right axis).

point of the lifting tail, or equivalently the front edge of the RSR_{acc} and denoted by χ_{RSR} hereafter. The χ_{RSR} for systems with $M_s = 1.43$, 1.54, 1.83 and 2.22 is indicated in figure 12(*a*) and gradually moves downstream with increased M_s consistent with the narrowing trend of the lifting tail with M_s. The χ_{RSR} is not discernible in cases with the weakest incident shocks, such as $M_s = 1.09$ and 1.17. The tail rising rate $\partial_\chi V^*_{tail}$ is calculated as the average variation of $V^*(\chi)$ per unit χ within the width of the RSR_{acc}, $\Delta\mathrm{RSR}_{acc}$, as follows:

$$\partial_\chi V^*_{tail} = \frac{V^*_{\chi=1} - V^*_{\chi_{RSR}}}{V^*_{\chi_{RSR}} \cdot \Delta\mathrm{RSR}_{acc}}, \tag{4.2}$$

where $V^*_{\chi=1}$ and $V^*_{\chi_{RSR}}$ represent the velocities at the rear surface and $\chi = \chi_{RSR}$, respectively, $\Delta\mathrm{RSR}_{acc} = 1 - \chi_{RSR}$. Figure 12(*b*) shows the variations in χ_{RSR} and $\partial_\chi V^*_{tail}$ with increasing M_s and unvaried Π, $\Pi = 0.5$. The χ_{RSR} first quickly moves downstream as the incident shock transitions from weak to strong and then converges to $\sim$0.7 after $M_s > 2$;
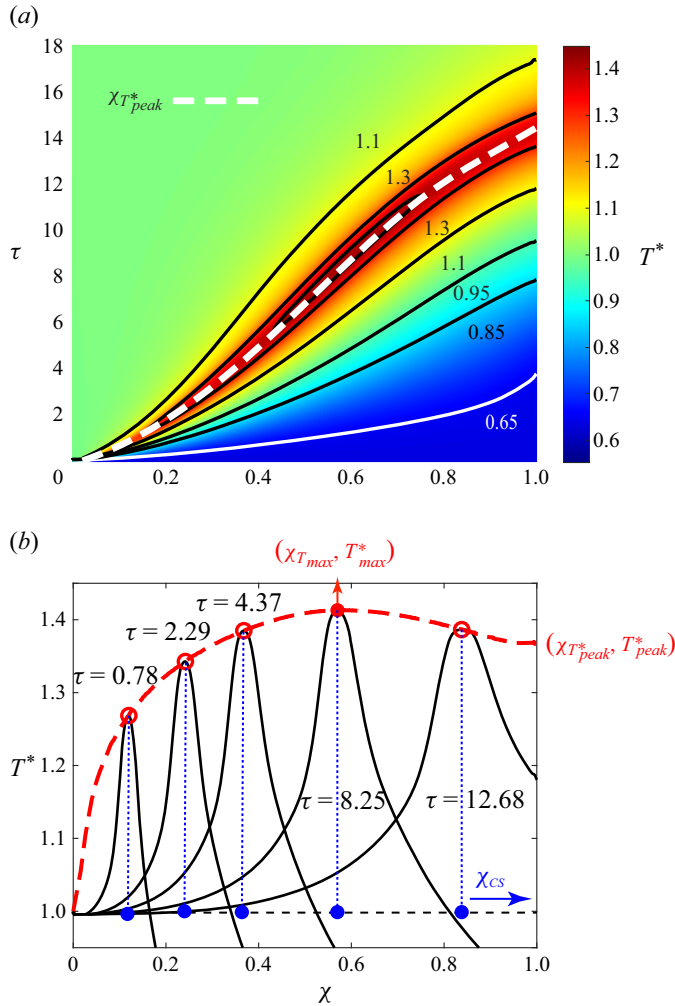
Figure 13. (*a*) Temporospatial evolution of the non-dimensional temperature field T^* for C-1.43-50. (*b*) Profiles $T^*(\chi)$ at sequential times enveloped by the evolution line of T^*_{peak} which reaches T^*_{max} at $\chi = \chi_{T^*_{max}}$. At every moment, the position of the temperature peak, $\chi_{T^*_{peak}}$, coincides with the position of the contact surface particle, χ_{CS}.

this result indicates a lower limiting width of the RSR_{acc}, $\Delta RSR_{acc} = 0.3$. Moreover, the tail rising rate $\partial_\chi V^*_{tail}$ continues to increase. From $M_s = 1.4$ to $M_s = 3$, $\partial_\chi V^*_{tail}$ increases almost tenfold.

4.3. *Gas temperature*

Figure 13(*a*) displays the temporospatial evolution of the non-dimensional temperature field, $T^* = T/T_5$, for C-1.43-50. Notably, there is a downstream-travelling hot gas layer whose temperature is considerably higher than T_5 and continues to increase. The profiles $T^*(\chi)$ at sequential times shown in figure 13(*b*) manifest the diffusive nature of the hot gas layer which spreads out while traversing the length of the column. The envelope of the peaks in the profiles $T^*(\chi)$ indicated by the red curve in figure 13(*b*) shows the variation in the peak temperature T^*_{peak} as a function of χ. For C-1.43-50, the hot gas layer undergoes
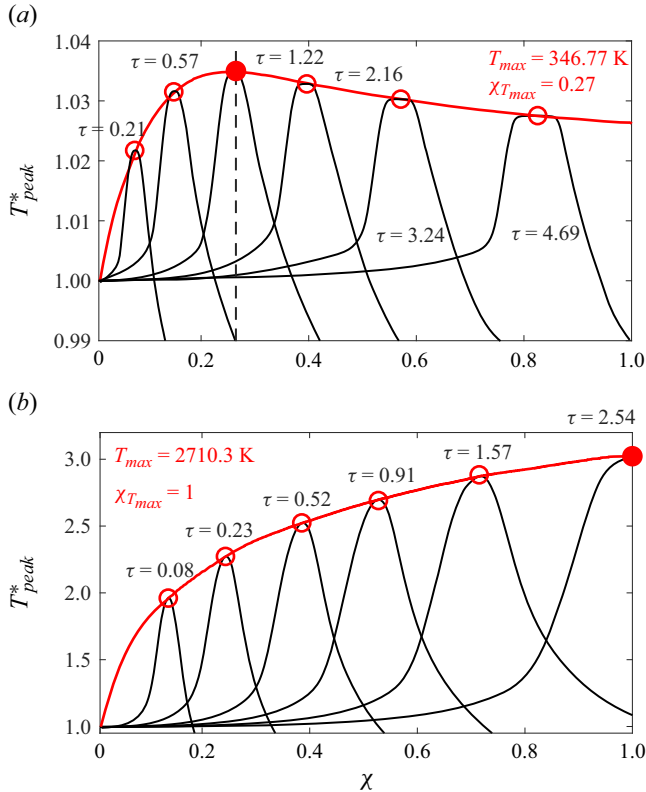
999 A91-18

Figure 14. Profiles $T^*(\chi)$ for C-1.09-50 (*a*) and C-2.22-0.045 (*b*). Envelopes of the temperature peaks at sequential times represent the variations in T^*_{peak}.

a substantial self-heating phase until it travels midway through the column when T^*_{peak} reaches its maximum T^*_{max}. The corresponding location of the temperature peak is denoted as $\chi_{T^*_{max}}$.

The trajectory of the temperature peak, $\chi_{T^*_{peak}}$, is depicted in $\chi-\tau$ space as indicated by the dashed line in figure 13(*a*). Another important trajectory is that of the contact surface, χ_{CS}, which separates the initial interstitial gases and infiltrated gases flowing from upstream. Note that the trajectory of the contact surface is actually the trace line of the first gas particle flowing into the granular column upon shock impingement. The derivation of χ_{CS} is presented in Appendix B. As shown in figure 13(*b*), the positions of $\chi_{T^*_{peak}}$ and χ_{CS} coincide with each other at every moment, implying that the temperature peak resides upon the contact surface, or equivalently it is the very first gas particle flowing into the column that is the hottest one. The coincidence between $\chi_{T^*_{peak}}(\tau)$ and $\chi_{CS}(\tau)$ is further explored in § 4.4.

Two more distinct heating processes of the hot gas layers are shown in figure 14(*a*,*b*). For C-1.09-50 (see figure 14*a*), T^*_{peak} increases to its maximum near the front surface, $\chi_{T^*_{max}} = 0.27$, followed by a gently declining plateau. In this scenario, most parts of the granular column are subjected to T^*_{max} albeit the values of T^*_{max} are modest, $T^*_{max} = 1.035$. In contrast, for C-2.22-0.045, the increase in T^*_{peak} persists until the hot gas layer passes the rear surface, $\chi_{T^*_{max}} = 1$. We observe a singularly maximum temperature $T^*_{max} = 3.11$ at the rear surface.

The traversing hot gas layer introduces additional energy into the gas filtration, part of which fuels the pressure diffusion. The coupling between the thermal effect embodied by the self-heating hot gas layer and the pressure diffusion is elaborated in §4.4. The occurrence of thermal stress in granular materials exposed to rapid temperature changes is known as 'thermal shock'. In fact, the propagation of the hot gas layer within the material induces a sharp thermal shock to the local solid skeleton with a temperature amplitude as high as a few hundred degrees. This intense thermal shock can result in significant surface or internal damages to the material, including cracks, fractures and other forms of degradation. For instance, a solid skeleton made of aluminium alloys loses almost its entire strength under thermal shock with an amplitude of 500 °C (Yin *et al.* 2023). Throughout the granular column the thermal shock markedly varies from part to part as indicated by the variation in T^*_{peak} in figures 13(*b*) and 14, which causes a mismatch of the resulting thermal stresses and thermal expansion. The property degradation in combination with the mismatching thermal stresses poses a great threat to the structural integrity of the solid skeleton. Consequently, the shock resistance performance of the granular medium probably deteriorates. Therefore, the thermal resistance properties of porous materials as candidates for shock protection shields need to be among the primary concerns when assessing the overall shock resistance performance.

Parameters T^*_{max} and $\chi_{T^*_{max}}$ are reasonable to use as the quantitative descriptors of the thermal effect of gas filtration. The former characterizes the intensity of the thermal effect while the latter measures the streamwise uniformity of the thermal effect. The contour maps of T^*_{max}, T_{max} and $\chi_{T^*_{max}}$ in the parameter space (M_s, Π) are shown in figure 15(*a–c*), respectively. A distinctive but resembling pattern can be identified from these contour maps. In general, a stronger incident shock causes a more intense and prolonged self-heating of the hot gas layer, especially in the strong incident shock domain $M_s > 2$. If we set the 10 % increase of the ambient temperature to 327.8 K as the upper limit of T_{max} below which the isothermal assumption holds, the corresponding threshold of $M_{s,iso}$ is 1.08, as shown in figure 15(*b*). Note that the M_s dependences of T^*_{max}, T_{max} and $\chi_{T^*_{max}}$ are substantially amplified in the domain with strong shocks, $M_s > 2$, and median levels of Π, $\Pi \sim O(10^{-3})$–$O(10^{-1})$.

In contrast with the monotonic increase in these parameters with M_s, the Π dependences are more complicated. In the domain of the weakest incident shock, $M_s < 1.1$, the isolines are parallel to the Π axis, indicating a minimum Π effect. As the incident shock strengthens, a nonlinear dependence of Π emerges and becomes increasingly prominent. For a given M_s ($M_s > 1.8$), T^*_{max} and T_{max} reach their maxima in the neighbourhood of $\Pi \sim O(10^{-2})$. Moreover, the completion of self-heating is delayed on the rear surface, $\chi_{T^*_{max}} = 1$. The resemblance of the variation patterns in T^*_{max} and $\chi_{T^*_{max}}$ indicates an explicit correlation between the heating intensity and the duration for which self-heating occurs. Specifically, the delay of the temperature convergence corresponds to an elevated maximum temperature. The hot gas layer is able to obtain a higher T^*_{max} if self-heating continually persists to the rear surface. In §4.5, we further account for the variation in $\chi_{T^*_{max}}$ in the M_s–Π parameter space in terms of the heating modes.

4.4. *Coupling between the thermal effect and the pressure diffusion*

The influence of the thermal effect on the pressure diffusion depends on the amount of heat carried by the hot gas layer which can be converted into the pressure potential. The total heat and the conversion proportion both play a significant role. We employ the time integral of the heat flux passing through the rear surface as a measurement of the total
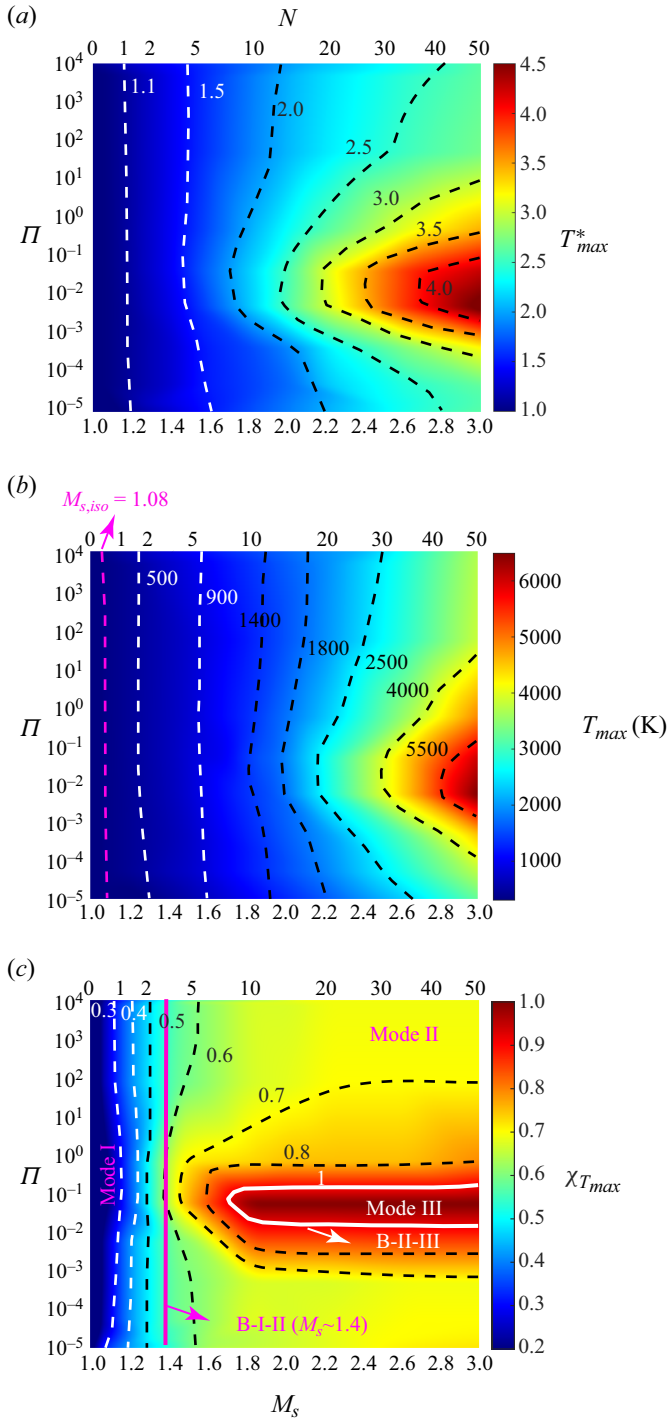
Figure 15. Contour maps of T^*_{max} (a), T_{max} (b) and $\chi_{T^*_{max}}$ (c) in the parameter space (M_s, Π). Three distinct heating modes, mode I: the gas-filtration-dominated mode, mode II: the rear-surface-dominated mode and mode III: persistent heating mode, are delineated by two boundaries. Boundaries between different modes are represented by the pink and white solid lines which are denoted as B-I-II and B-II-III, respectively.
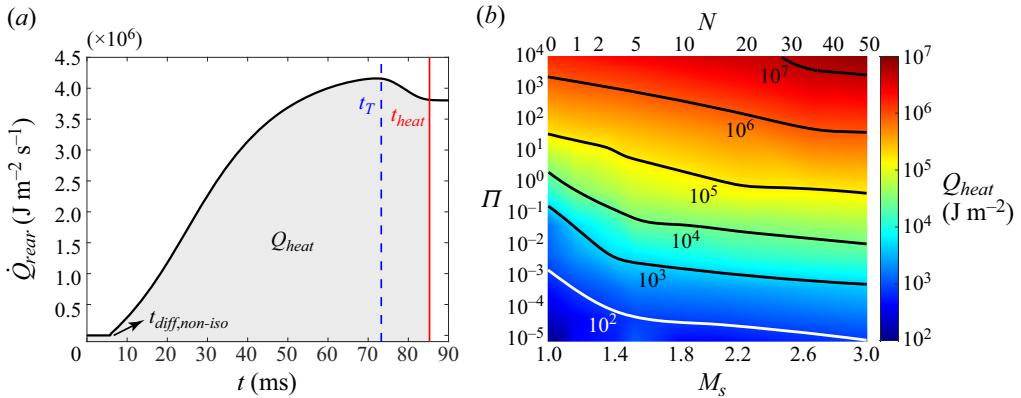
Figure 16. (*a*) Temporal variation in $\dot{Q}_{rear}$ prior to a steady heat flux being established for C-1.43-50. (*b*) Contour map of Q_{heat} in the parameter space (M_s, Π).

heat. The heat flux at the rear surface, $\dot{Q}_{rear}$, is calculated as follows:

$$\dot{Q}_{rear} = \rho_{rear} e_{rear} V_{rear}, \tag{4.3}$$

where ρ_{rear}, e_{rear} and V_{rear} are the gas density, specific internal energy and gas velocity at the rear surface, respectively. Here e_{rear} is a function of the gas temperature at the rear surface, $e_{rear} = c_v T_{rear}$, where c_v is the constant-volume specific heat capacity. Substituting $e_{rear} = c_v T_{rear}$ and the equation of state for the ideal gases, $P_{rear} = \rho_{rear} R T_{rear}$, into (4.3), (4.3) reduces to the following:

$$\dot{Q}_{rear} = \frac{1}{\gamma - 1} P_{rear} V_{rear}. \tag{4.4}$$

Figure 16(*a*) shows evolution of $\dot{Q}_{rear}$ for C-1.43-50. When the diffusing pressure field front arrives at the rear surface, $\chi_p = 1$ ($t_{diff,non-iso} = 5.78$ ms), $\dot{Q}_{rear}$ begins to increase until the contact surface particle passes through the rear surface ($t_T = 72.0$ ms) when $\dot{Q}_{rear}$ reaches the maximum. Afterwards the $\dot{Q}_{rear}$ curve drops slightly before converging to a steady value at $t_{heat} = 85.3$ ms. If we assume that thermal effect diminishes as the hot gas layer moves to the rear surface, the total heat relevant to the thermal effect, Q_{heat}, can be calculated as the integral of the $\dot{Q}_{rear}(t)$ curve from $t_{diff,non-iso}$ to t_{heat}:

$$Q_{heat} = \int_{t_{diff,non-iso}}^{t_{heat}} \dot{Q}_{rear} \, dt. \tag{4.5}$$

The contour map of Q_{heat} in the parameter space (M_s, Π) is shown in figure 16(*b*). The dependence of Q_{heat} on Π overpowers its dependence on M_s. Hence, the isolines exhibit a horizontally tilted pattern. As Π increases from $O(10^{-5})$ to $O(10^4)$, Q_{heat} increases over five decades.

The proportion of Q_{heat} contributing to pressure diffusion depends on the ratio between the traversal time of the hot gas layer, τ_T, and the characteristic time of the pressure diffusion, $\xi_T = \tau_T / \tau_{diff,non-iso}$. The contour map of ξ_T in the parameter space (M_s, Π) is shown in figure 17(*a*); a strong dependence on M_s in the weak incident shock domain, $M_s < 1.6$, is observed, and Π plays a more important role in the strong incident shock domain, $M_s \geq 1.6$. Inside the upper right corner of the parameter space delineated by the
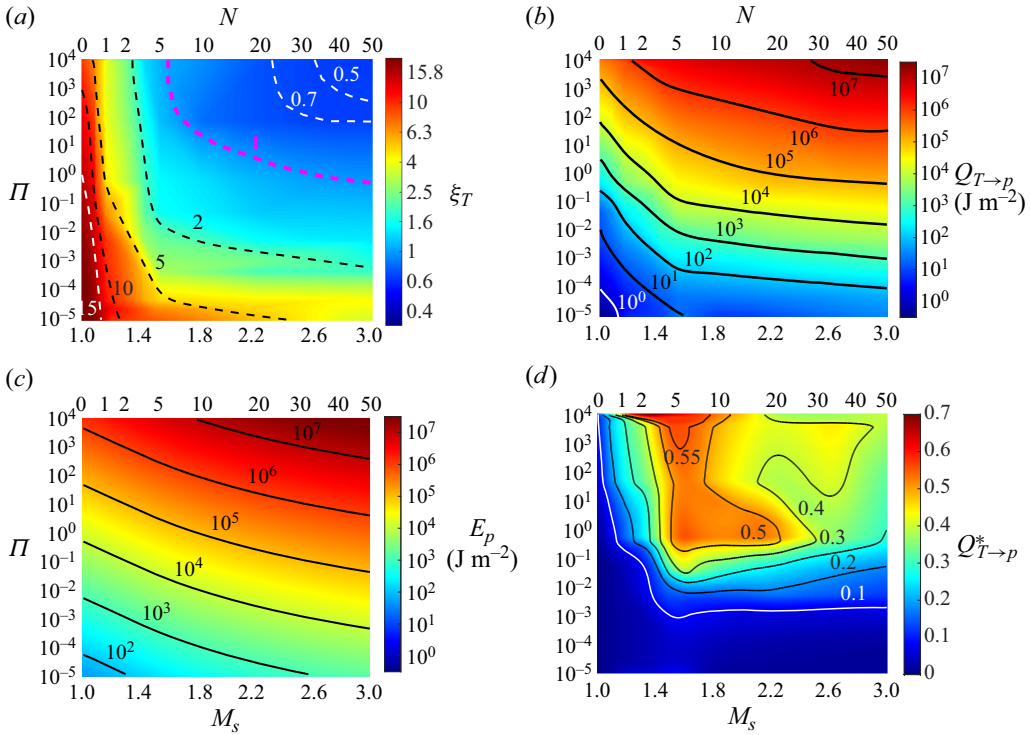
Figure 17. Contour maps of ξ_T (a), $Q_{T \to p}$ (b), E_p (c) and $Q_{T \to p}^*$ (d) in the parameter space (M_s, Π).

isoline $\xi_T = 1$ (see figure 17a), the hot gas layer travels faster than the pressure diffusion; therefore, almost all Q_{heat} is available for expediting the pressure diffusion. Otherwise, the cumulative heat flux in the duration of $\tau_{diff,non\text{-}iso}$ possibly contributes to a faster pressure diffusion. The inverse of ξ_T serves as a scale factor measuring the proportion of Q_{heat} fuelling the pressure diffusion. The heat available for conversion into the pressure potential, $Q_{T \to p}$, is a function of Q_{heat} as well as ξ_T:

$$\left. \begin{aligned} Q_{T \to p} &= Q_{heat} \quad \text{for } \xi_T < 1, \\ Q_{T \to p} &= Q_{heat}/\xi_T \quad \text{for } \xi_T \geq 1. \end{aligned} \right\} \tag{4.6}$$

Figure 17(b) shows the contour map of $Q_{T \to p}$ which has a similar pattern to Q_{heat}. Specifically, the isolines of $Q_{T \to p}$ take the form of a semi-parallel inclined line in the weak incident shock domain, $M_s < 1.6$, while they transition into a series of semi-horizontal lines in the strong incident shock domain, $M_s \geq 1.6$.

A non-dimensional $Q_{T \to p}$, $Q_{T \to p}^* = Q_{T \to p}/E_p$, is employed to better characterize the thermal effects on the pressure diffusion, where E_p is the cumulative pressure potential energy along the length of the granular column subject to the steady diffusing pressure field:

$$E_p = \int_0^l P(x) \, dx. \tag{4.7}$$

Figure 17(c) plots the contour map of E_p in the parameter space (M_s, Π) wherein the isolines take the form of regularly spaced parallel lines slowly inclining from the upper left

towards the lower right. For C-1.43-50, $Q^*_{T\rightarrow p} = 0.42$ with $Q_{T\rightarrow p} = 1.37 \times 10^5$ J m^{-2} and $E_p = 3.19 \times 10^5$ J m^{-2}, indicating the heat available to fuel the pressure diffusion is 42 % of the pressure potential. The contour map of $Q^*_{T\rightarrow p}$ calculated as the ratio between $Q_{T\rightarrow p}$ and E_p is shown in figure 17(*d*); this displays convoluted isolines with the highest value $Q^*_{T\rightarrow p} \sim 0.7$ appearing in the region as Π approaches the upper limit, $\Pi \sim O(10^4)$, while the incident shock is relatively weak, $M_s \sim 1.3$. Notably, the bottom region of figure 17(*d*) enclosed by the isoline $Q^*_{T\rightarrow p} = 0.1$ roughly coincides with the upper boundary of TR_{diff}. Indeed, beneath the isoline $Q^*_{T\rightarrow p} = 0.1$, the heat flux contributing to diffusion is trivial relative to the pressure potential which is the primary driving force for diffusion. Accordingly, the pressure diffusion therein is barely affected.

4.5. *Mechanisms underlying the thermal effect*

In this section, the heating mechanism governing the temperature evolution of the traversing hot gas layer is accounted for from the perspective of energy conservation. In the Lagrangian frame, the internal energy conservation equation for an individual gas particle is as follows:

$$\rho_g \frac{R}{\gamma - 1} \frac{dT}{dt} = \frac{1 - \varepsilon}{\varepsilon} \rho_g D_p V_g^2 - P \frac{\partial V_g}{\partial x}. \tag{4.8}$$

The term on the left-hand side of (4.8) represents the growth rate of the internal energy per unit volume. The variation in the internal energy is related to the viscous dissipation caused by the drag force between the gas and solid skeleton (the first term on the right-hand side) as well as unsteady pressure work (the second term on the right-hand side). Viscous dissipation always leads to gas heating. In contrast, the contribution of the pressure work to the gas internal energy depends on the sign of the streamwise velocity gradient. Specifically, accelerating gases undergoing expansion are doing work to the surroundings at the expense of the internal energy. Otherwise, decelerating gases are heated up along with being compressed. Thus, whether gas heating occurs depends on the nature (expansion or compression) and magnitude of the pressure work relative to viscous dissipation. Gas heating is terminated only when the gas particle commences a sufficiently strong acceleration phase. A maximum temperature is observed inside the granular column. Otherwise, the gas particle's temperature continuously increases until it passes through the rear surface.

To better illustrate the dependence of the thermal effect on the flow and thermodynamic parameters, we substitute the drag force model, namely the Di Felice model ((2.4)–(2.7)), and the non-dimensional variables defined in (2.20) into (4.8). Hence, (4.8) reduces to its non-dimensional form:

$$\frac{dT^*}{d\tau} = \frac{N(\gamma - 1)}{N + 1} \frac{\mu^*}{\rho^*_{non\text{-}iso}} (V^*_{non\text{-}iso})^2 + \frac{N(\gamma - 1)}{N + 1} N\Pi \frac{\rho_5}{\rho_1} (V^*_{non\text{-}iso})^3$$
$$- \frac{N\theta_{non\text{-}iso} + 1}{N + 1} \frac{\gamma - 1}{\rho^*_{non\text{-}iso}} \frac{\partial V^*_{non\text{-}iso}}{\partial \chi}, \tag{4.9}$$

where μ^* is the non-dimensional dynamic viscosity, $\mu^* = \mu_g/\mu_1$, and the non-dimensional density ρ^* satisfies the non-dimensional equation of state for ideal gases:

$$\rho^*_{non\text{-}iso} = \frac{N\theta_{non\text{-}iso} + 1}{N + 1} \frac{1}{T^*}. \tag{4.10}$$
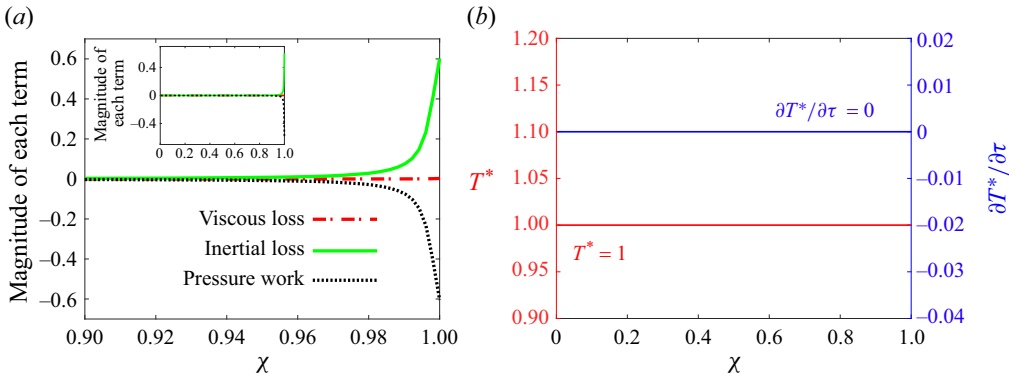
Figure 18. (*a*) Zoom-in plot ($\chi > 0.9$) of the streamwise variations in the viscous loss, inertial loss and pressure work during the steady diffusion phase for C-2.99-5000. Inset: the whole streamwise profiles of each term. (*b*) Corresponding temperature growth rate and temperature distribution along the length of the granular column.

The first and second terms on the right-hand side of (4.9) represent the (linear) viscous and (nonlinear) inertial losses of the viscous dissipation, respectively. As indicated in (4.9), the variation rate of the gas temperature depends on the instantaneous values of the velocity, $V^*_{non-iso}$, the velocity gradient, $\partial_\chi V^*_{non-iso}$, the pressure, $\theta_{non-iso}$, and the density, $\rho^*_{non-iso}$.

For low-speed gas filtration without the compressible effect, the gaseous density $\rho^*_{non-iso}$ remains consistent from the upstream all the way down to the downstream. As a result, T^* is proportional to $\theta_{non-iso}$ which monotonically decays with distance from the upstream surface. Thus, no gas heating is expected. For isothermal gas filtration with the compressible effect which does not allow the upstream temperature to differ from the downstream one, there is no temperature variation ($dT^*/d\tau = 0$). Equation (4.9) reduces to the compressible version of the Forchheimer law, whereby the linear and nonlinear flow resistance forces as well as the unsteady pressure work are all taken into account.

We first address the non-existence of the thermal effect during the steady pressure diffusion phase during which the temperature field is uniform and consistent with T_5. As illustrated in figure 10, the converged velocity profile, $V^*_{non-iso}(\chi)$, of the steady flows has a form of a gently upwards slope with (in the strong incident shock domain) or without (in the weak incident shock domain) a lifting tail. The overall low magnitude and flatness of the profile $V^*_{non-iso}(\chi)$ except for the lifting tail indicate that the gas particles flow through the bulk of the granular column at relatively low and unvaried velocities. Hence, outside the RSR$_{acc}$ all three terms on the right-hand side of (4.9) become negligible such that the gas temperature remains constant. If the profile $V^*_{non-iso}(\chi)$ features a significant lifting tail, the gas particles undergo a substantial acceleration as they pass through the RSR$_{acc}$, and the viscous dissipation and the expansion work are equally intense such that the resulting heating and cooling effects may be effectively negated. As a result, the gas temperature barely changes across the RSR$_{acc}$. Figure 18 shows the streamwise variations in each of the three terms on the right-hand side of (4.9) during the steady diffusion phase for C-2.99-5000 which is supposed to manifest the strongest thermal effect. The viscous loss (the first term) of the viscous dissipation remains minimal which is consistent with the Forchheimer flow characteristic of gas filtration in this case with $Re_f = 2.5 \times 10^5$. The inertial loss and pressure work terms, albeit having non-trivial values, offset each other due to opposite signs leading to a neutralized temperature growth rate as shown in figure 18(*b*). No thermal effect in terms of detectable heating or cooling effects can be observed during the steady filtration phase.
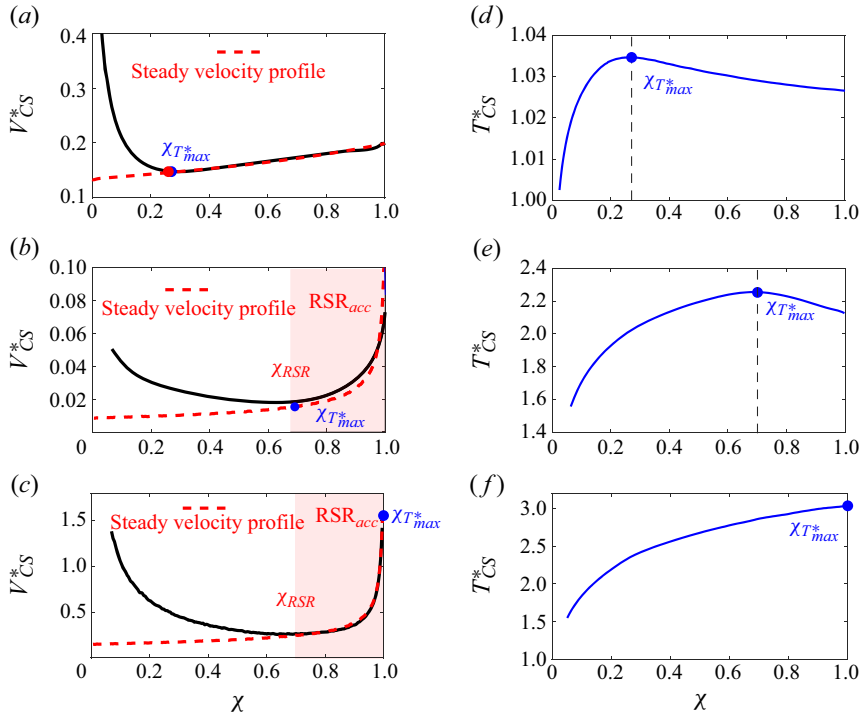
Figure 19. Comparisons of the contact surface particle's velocity evolutions $V_{CS}^*(\chi)$ and converged velocity profiles $V_{non-iso}^*(\chi)$ for C-1.09-50 (*a*), C-2.22-50 (*b*) and C-2.22-0.045 (*c*). Profile $V_{CS}^*(\chi)$ for C-0.5-50 deflects upon the steady diffusing pressure fields is established and marked by the red circle in (*a*). The front edges of the RSR$_{acc}$ for C-2.22-50 and C-2.22-0.045 are also indicated in (*b,c*) by χ_{RSR}. Profiles $T_{CS}^*(\chi)$ corresponding to (*a–c*) are shown in (*d–f*), respectively. The locations of $T_{max}^*(\chi)$ are denoted by $\chi_{T_{max}^*}$ marked in each panel.

In contrast to the steady flows during the steady filtration phase, gas particles flow through the column at relatively high and markedly varying velocities during the incipient filtration phase as indicated in figure 10. Accordingly, the viscous dissipation and the pressure work in this phase play a non-trivial role, producing intensified thermal effects. The very first gas particle that flows into the granular column upon shock impingement, namely the contact surface particle, attains the highest velocities and undergoes the most significant velocity fluctuation. Figure 19(*a–c*) shows a comparison of the velocity evolutions of the contact surface particle, $V_{CS}^*(\chi)$, and the converged velocity profiles for C-1.09-50, C-2.22-50 and C-2.22-0.045, respectively; considerable differences, especially in the first half of the column, are observed. Consequently, the contact surface particle is subjected to the most intensified heating. The trace line of the contact surface particle forms the hottest contour line in the temperature field T^* as shown in figure 13(*a*).

For C-1.09-50 the temperature of the contact surface particle, $T_{CS}^*(\chi)$, reaches its maximum at the deflection point of the profile $V_{CS}^*(\chi)$ as shown in figure 19(*d*), $\chi_{T_{max}^*} = 0.27$. Actually, the $V_{CS}^*(\chi)$ curve beyond $\chi_{T_{max}^*} = 0.24$ coincides with the converged velocity profile since the steady flows are well developed when the contact surface particle reaches $\chi_{T_{max}^*}$. Gas self-heating is terminated by the premature formation of the steady flows, which occur in cases where the filtrated gas particles lag far behind the pressure diffusion front, $\xi_T \sim O(10^1)$. Since there is no gas acceleration towards the rear surface, we refer to this heating mode as the gas-filtration-dominated mode.

999 A91-26

For C-2.22-50 and C-2.22-0.045, both of which have noticeable RSR_{acc}, the maximum temperatures of the contact surface particles are attained at the front edge of RSR_{acc}, $\chi_{T^*_{max}} = \chi_{RSR}$, and the rear surface, $\chi_{T^*_{max}} = 1$, respectively. Since the heating effect associated with the viscous dissipation and the 'cooling effect' caused by the expansion work are both active inside the RSR_{acc}, $\chi_{T^*_{max}} = \chi_{RSR}$ indicates that the cooling effect prevails while $\chi_{T^*_{max}} = 1$ means that the heating effect dominates throughout. The cases wherein the cooling effect inside the RSR_{acc} suffices to reverse the persistent gas heating, such as C-2.22-50, are referred to as the rear-surface-dominated heating mode. Otherwise, the gases are continually heated to the rear surface in cases such as C-2.22-0.045, which are referred to as the persistent heating mode.

The boundaries delineating these three distinct heating modes are superimposed on the contour map of $\chi_{T^*_{max}}$ in figure 15(c). The boundary between the gas-filtration- and rear-surface-dominated modes roughly aligns with the vertical line $M_s \sim 1.4$ which coincides with the isoline of $\xi_T = 2$ as indicated in figure 17(a). In the gas-filtration-dominated domain the gas temperature reaches T^*_{max} in the first half of the granular column and gradually decreases as the gases flow downstream. The persistent heating mode resides in the narrow band enveloped by the vertical line $M_s \sim 1.8$, and two horizontal lines $\Pi \sim 10^{-2}$ and $\Pi \sim 10^{-1}$. The remaining region in the M_s–Π space belongs to the rear-surface-dominated domain, where T^*_{max} is reached inside the RSR_{acc}. Upon closer inspection of figure 15(a,c), the presence of the persistent heating domain evidently warps the contour lines of T^*_{max} and T_{max} therein such that $T^*_{max}(\Pi)$ and $T_{max}(\Pi)$ display significant nonlinear behaviours across the persistent heating domain.

The location of the persistent heating domain in the parameter space (M_s, Π) can be predicted via (4.9). The viscous loss (first term on the right-hand side), the inertial loss (second term on the right-hand side) and the pressure work (third term on the right-hand side) scale with $(V^*_{non\text{-}iso})^2$, $N\Pi(V^*_{non\text{-}iso})^3$ and $\partial_\chi V^*_{non\text{-}iso}$, respectively. Employing $V^*_{\chi_{RSR}}$ and the average gradient of $V^*(\chi)$ within ΔRSR_{acc} as approximations of $V^*_{non\text{-}iso}$ and $\partial_\chi V^*_{non\text{-}iso}$, respectively, gives the following:

$$\partial_\chi V^*_{non\text{-}iso} = \frac{\partial V^*_{non\text{-}iso}}{\partial \chi} = \frac{V^*_{\chi=1} - V^*_{\chi_{RSR}}}{\Delta RSR_{acc}}. \tag{4.11}$$

We plot each term's variations with Π at $M_s = 1.43$ and 2.22 as shown in figure 20(a,b). For both cases the viscous loss overwhelms the inertial loss in the domain with $\Pi \leq O(10^{-1})$ and $Re_f \leq O(10^0)$ corresponding to the Darcy flow regime. As Π exceeds $O(10^{-1})$, the Forchheimer flow begins to develop, and the inertial loss becomes dominant. Hence, whether gas self-heating is sustained across RSR_{acc} ($dT^*/d\tau > 0$) depends on the relative importance of the pressure work and the viscous loss ($\Pi \leq O(10^{-1})$) or the inertial loss ($\Pi > O(10^{-1})$). For the strong incident shock, $M_s = 2.22$, the value of viscous loss exceeding the absolute value of the (expansion) pressure work only occurs within a narrow interval of Π, $O(10^{-2}) < \Pi < O(10^{-1})$ (see figure 19a), wherein the persistent heating mode dominates. Beyond this interval of Π, the pressure work always prevails over either the viscous loss ($\Pi \leq O(10^{-1})$) or the inertial loss ($\Pi > O(10^{-1})$). The gas heating is halted within the RSR_{acc}. The rear-surface-dominant heating mode is also the sole heating mode for $M_s = 1.43$ regardless of Π since the pressure work inside the RSR_{acc} is always higher than the viscous and internal losses (see figure 20b). The predicted location of the persistent heating domain in the parameter space (M_s, Π) is consistent with the numerically derived phase diagram shown in figure 15(a).
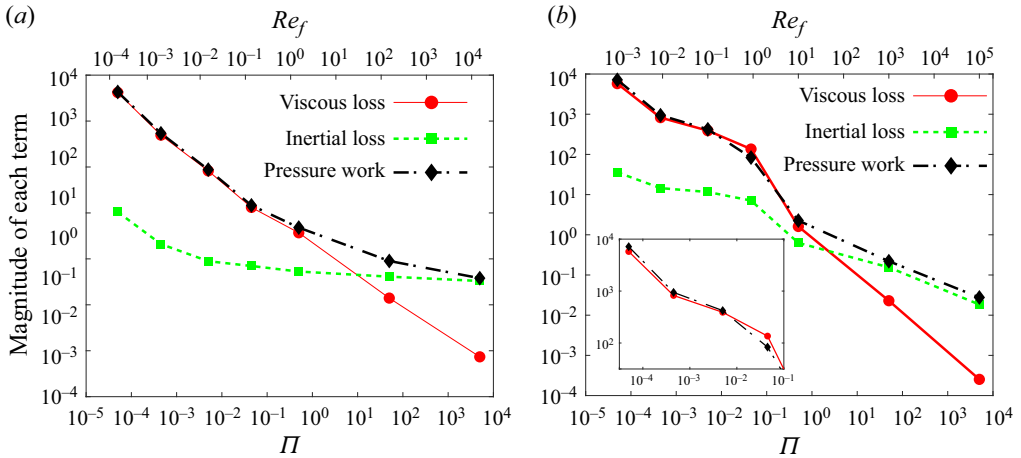
Figure 20. Variations in the magnitudes of the viscous loss, inertial loss and pressure work with Π at $M_s = 1.43$ (*a*) and 2.22 (*b*). Inset of (*b*): zoom-in plot of the variations in magnitude of each term in the domain with $\Pi \leq O(10^{-1})$.

5. Discussion

The relation between the non-isothermal gas density, $\rho^*_{non\text{-}iso}$, and the non-isothermal temperature, $T^*_{non\text{-}iso}$, as well as the non-isothermal pressure, $\theta_{non\text{-}iso}$, is shown in (4.10). Differentiating (4.10) with respect to χ enables the correlation of the spatial variation of $\rho^*_{non\text{-}iso}$ with $T^*_{non\text{-}iso}$ and $\theta_{non\text{-}iso}$ as given in (5.1):

$$\frac{\partial \rho^*_{non\text{-}iso}}{\partial \chi} = \frac{1}{(N+1){T^*_{non\text{-}iso}}^2} \left[NT^*_{non\text{-}iso} \frac{\partial \theta_{non\text{-}iso}}{\partial \chi} - (N\theta_{non\text{-}iso} + 1)\frac{\partial T^*_{non\text{-}iso}}{\partial \chi} \right]. \quad (5.1)$$

Since $\theta_{non\text{-}iso}$ monotonically decays with χ, $\partial_\chi \theta_{non\text{-}iso} < 0$ and whether $\rho^*_{non\text{-}iso}$ similarly decays with χ depends on the sign and magnitude of $\partial_\chi T^*_{non\text{-}iso}$. Note that the coefficients in the two derivative terms on the right-hand side of (5.1), $NT^*_{non\text{-}iso}$ and $N\theta_{non\text{-}iso} + 1$, are of the same order of magnitude. Figure 21 shows the characteristic profiles $\rho^*_{non\text{-}iso}$ and $T^*_{non\text{-}iso}(\chi)$ for C-3.5-50 at $\tau = 1.45$. On the rising side of the temperature peak, $\partial_\chi T^*_{non\text{-}iso} > 0$ such that $\rho^*_{non\text{-}iso}$ decreases with χ with a steeper slope than that of the isothermal density. On the declining side of the temperature peak, $\partial_\chi T^*_{non\text{-}iso} < 0$. If the absolute value of $\partial_\chi T^*_{non\text{-}iso}$, $|\partial_\chi T^*_{non\text{-}iso}|$, is in excess of that of $\partial_\chi \theta_{non\text{-}iso}$, $\partial_\chi \rho^*_{non\text{-}iso}$ becomes positive, resulting in a temporary increase in $\rho^*_{non\text{-}iso}$. As shown in figure 21(*a*) a depression appears in profile $\rho^*_{non\text{-}iso}(\chi)$ immediately downstream of the temperature peak, wherein $|\partial_\chi T^*_{non\text{-}iso}|$ is the largest. The $|\partial_\chi T^*_{non\text{-}iso}|$ becomes increasingly smaller with χ as the tail of the profile $T^*_{non\text{-}iso}(\chi)$ spreads out and eventually is surpassed by $|\partial_\chi \theta_{non\text{-}iso}|$. Afterwards the profile $\rho^*_{non\text{-}iso}(\chi)$ resumes the general decay characteristics.

The emergence of the evident temperature peak in the profile $T^*_{non\text{-}iso}(\chi)$ is the signature of the thermal effects. As mentioned before, the density depression in the profile $\rho^*_{non\text{-}iso}(\chi)$ is also the imprint of the thermal effects. The width and amplitude of the rising ramp of the density depression with positive $\partial_\chi \rho^*_{non\text{-}iso}$ show the influence of the thermal effects on the density field. We denote the starting and ending points of the positive $\partial_\chi \rho^*_{non\text{-}iso}$ phase as $\chi^0_{\partial\rho>0}$ and $\chi^1_{\partial\rho>0}$, respectively. The width of the positive $\partial_\chi \rho^*_{non\text{-}iso}$ phase, $\Delta\chi_{\partial\rho>0}$, is the interval between $\chi^0_{\partial\rho>0}$ and $\chi^1_{\partial\rho>0}$, $\Delta\chi_{\partial\rho>0} = \chi^1_{\partial\rho>0} - \chi^0_{\partial\rho>0}$.

999 A91-28
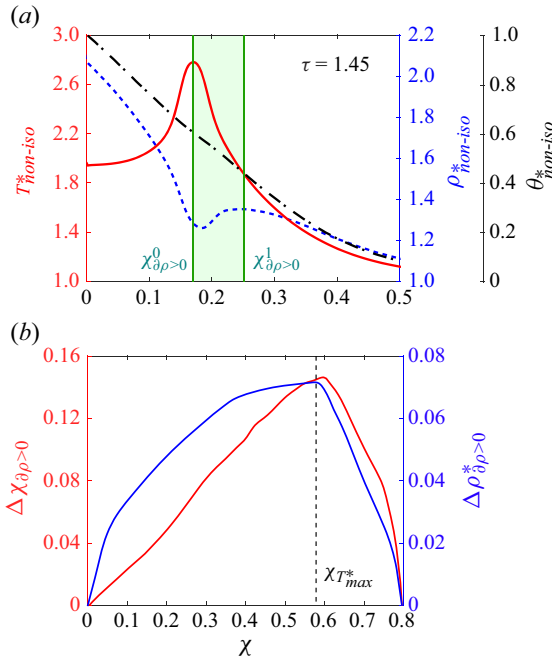
Figure 21. (*a*) Profiles of $\rho^*_{non\text{-}iso}$ (blue dashed line), $T^*_{non\text{-}iso}(\chi)$ (red solid line) and $\theta^*_{non\text{-}iso}(\chi)$ (black dash-dot line) for C-3.5-50 at $\tau = 1.45$. The shaded band indicates the region with a positive density gradient, $\partial_\chi \rho^*_{non\text{-}iso} > 0$. (*b*) Streamwise variations in the width and amplitude of the positive $\partial_\chi \rho^*_{non\text{-}iso}$ phase, $\Delta\chi_{\partial\rho>0}$ and $\Delta\rho^*_{\partial\rho>0}$ for C-3.5-50.

The amplitude of the positive $\partial_\chi \rho^*_{non\text{-}iso}$ phase is defined as $\Delta\rho^*_{\partial\rho>0} = \rho^*_{non\text{-}iso}(\chi^1_{\partial\rho>0}) - \rho^*_{non\text{-}iso}(\chi^0_{\partial\rho>0})$. Figure 21(*b*) shows the streamwise variations in $\Delta\chi_{\partial\rho>0}$ and $\Delta\rho^*_{\partial\rho>0}$ for C-3.5-50. As this case belongs to the rear-surface-dominated heating mode domain, the temperature peak becomes tempered inside the RSR$_{acc}$, indicating the waning of the thermal effects. As a result, the positive $\partial_\chi \rho^*_{non\text{-}iso}$ phase becomes increasingly narrower with reduced amplitude as shown in figure 21(*b*).

Figure 22(*a–c*) displays the temporospatial evolutions of $\rho^*_{non\text{-}iso}$ in C-1.09-50, C-1.43-50 and C-2.22-0.045, which belong to the gas-filtration-dominated, rear-surface-dominated and persistent heating domains, respectively. The temporospatial evolutions of the corresponding $\partial_\chi \rho^*_{non\text{-}iso}$ are shown in figure 22(*d–f*), respectively. The thermal effect in the gas-filtration-dominated heating mode is generally modest, shown by the slight temperature rise, as indicated in figure 14; this does not suffice to cause a positive $\partial_\chi \rho^*_{non\text{-}iso}$ phase, which is the case in C-1.09-50 (figure 22*a,d*). The amplified thermal effect in the rear-surface-dominated heating mode allows the presence of a positive $\partial_\chi \rho^*_{non\text{-}iso}$ phase downstream of the contact surface (figure 22*b,e*). However, the positive $\partial_\chi \rho^*_{non\text{-}iso}$ phase diminishes as it approaches the rear surface since the thermal effect attenuates in the RSR$_{acc}$. We observe a substantial enhancement of the positive $\partial_\chi \rho^*_{non\text{-}iso}$ phase in cases controlled by the persistent heating mode in terms of the intensity, expanse and outreach, as shown in figure 22. A sharp density gradient across the hot gas layer enables high-speed schlieren imaging to visualize the thermal effect in this scenario.

The misalignment of contour lines between $\theta_{non\text{-}iso}$ and $\rho^*_{non\text{-}iso}$ provides the source for the baroclinic torque, $\nabla\theta_{non\text{-}iso} \times \nabla\rho^*_{non\text{-}iso}$, which contributes to vorticity generation.
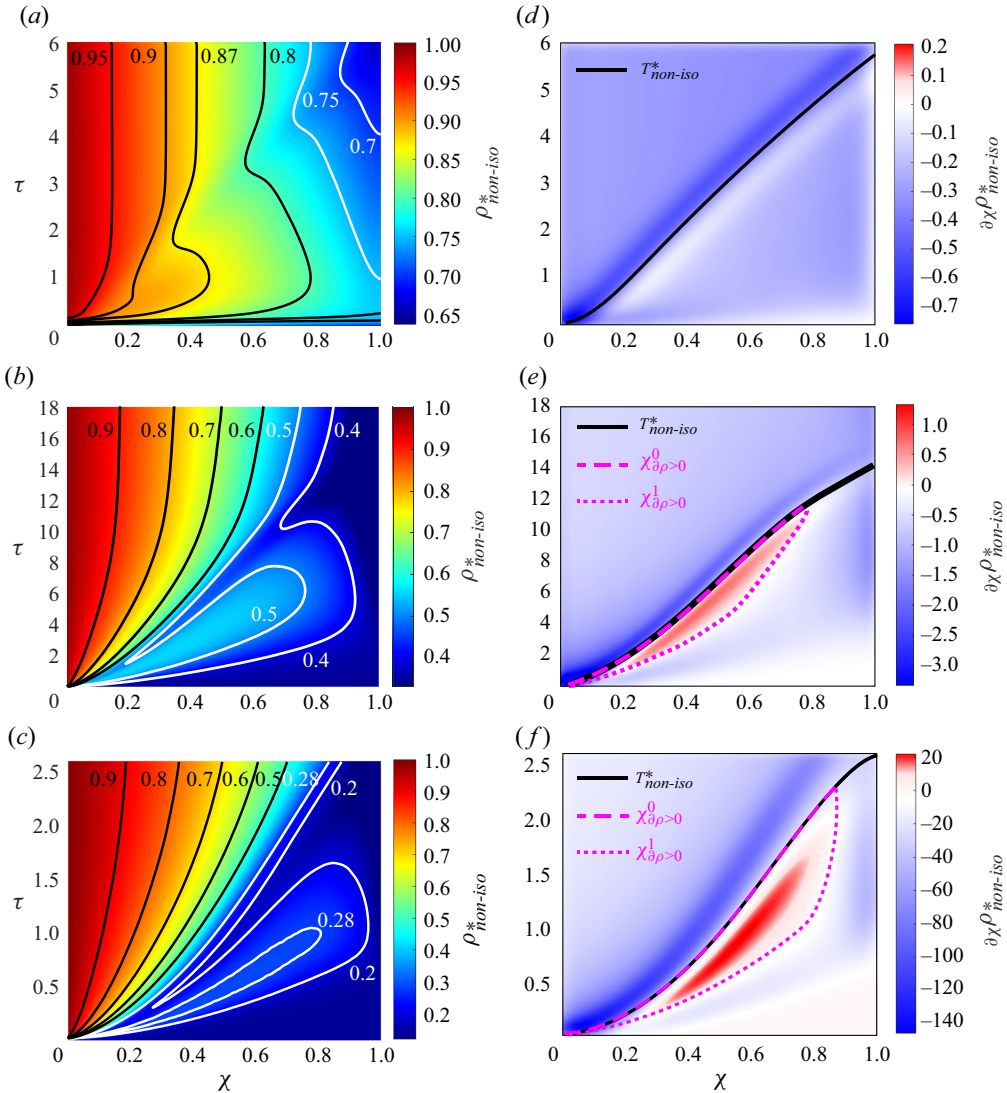
Figure 22. Temporospatial evolutions of $\rho^*_{non\text{-}iso}$ (a–c) and $\partial\chi\rho^*_{non\text{-}iso}$ (d–f) in C-1.09-50 (a,d), C-1.43-50 (b,e) and C-2.22-0.045 (c,f).

If the vortices become so profuse that the laminar flow assumption is challenged, the formulations of Morrison's method become problematic. For mobile particle packings, the baroclinic vorticity introduces momentum to the particles in the non-streamwise directions and is likely responsible for the clustering or 'channelling' of the particles through the vortices. The baroclinic vorticity caused by thermal effects needs to be considered in the theory of shock-driven multiphase instability, which primarily accounts for the drag-induced vorticity deposition.

6. Conclusion

We carried out a comprehensive numerical investigation of shock-induced gas filtration through rigid granular columns in parameter space constructed by two defining

non-dimensional parameters, namely the incident shock Mach number, M_s, and the filtration coefficient, Π. In contrast to the normally adopted isothermal gas filtration assumption, the results show an intense non-isothermal filtration process characterized by a self-heating gas layer traversing the column. The resulting thermal effects have two major implications. First, the pressure diffusion is accelerated due to the influx of the additional heat which depends on the cumulative heat flux and the time-scale ratio between the thermal effect and the pressure diffusion. Second, the heat spike associated with the hot gas layer results in an intense thermal shock which may pose a threat to the integrity of the solid skeleton. The maximum gas temperature and the corresponding location are of most concern in this regard; they are used to characterize the intensity and uniformity of the thermal effect, respectively. The contour maps of the thermal effects are constructed in the parameter space (M_s, Π) from these two perspectives.

The self-heating mechanisms of the hot gas layer are considered in energy analysis. The thermal effects are further classified into three distinct modes based on the dominant heat mechanisms: gas-filtration-dominated, rear-surface-dominated and persistent heating modes. The phase diagram of the heating modes is also established in the parameter space (M_s, Π). Each heating mode correlates with distinct characteristics of the thermal effects, which justifies the variations in the thermal effects with M_s and Π.

Glossary

English letters

Parameter	Explanation	Unit
a	Darcy coefficient	m^{-2}
b	Forchheimer coefficient	m^{-1}
c	sound speed	m s^{-1}
C_d	dimensionless drag force coefficient	—
d	diameter	m
D_p	drag force coefficient	m^{-1}
e	specific internal energy per unit mass	J kg^{-1}
e_p	restitution coefficient	—
E	total energy per unit mass	J kg^{-1}
E_p	cumulative pressure potential energy along the length of the granular column subject to the steady diffusing pressure field	J m^{-2}
F	force	N
F_C	collision force	N
k	permeability of particle column	m^2
k_n	stiffness coefficient	N m^{-1}
l	length of particle column and the length scale	m
m	mass	kg
M_s	Mach number of incident shock	—
N	non-dimensional intensity of the pressure impact	—
P	pressure	Pa
P_1	atmospheric pressure	Pa
P_5	reflected pressure of the incident shock	Pa
Q_{heat}	total heat relevant to the thermal effect	J m^{-2}
$\dot{Q}_{rear}$	heat flux at the rear surface	$\text{J m}^{-2}\,\text{s}^{-1}$
$Q_{T \to p}$	heat available for being converted into the pressure potential	J m^{-2}
r	radius	m

Parameter	Explanation	Unit
Re_f	effective Reynolds number	—
sg	specific weight	—
t	time	s
t_{diff}	time diffusing pressure field front arrives at the rear surface	s
t_T	time contact surface particle passes through the rear surface	s
t_{heat}	time heat flux at the rear surface converging to a steady value	s
t_{sc}	characteristic time scale	s
T	temperature	K
T_{CS}^*	temperature of the contact surface particle	—
T_{peak}^*	peak flow temperature in the temperature profile	—
T_{max}	maximum flow temperature in the particle column	K
T_1	ambient temperature	K
T_5	temperature of the reflected shock upstream	K
T_5^*	non-dimensional upstream temperature	—
u	velocity	m s^{-1}
$\bar{u}_f$	average fluid velocity at the location of a particle	m s^{-1}
$\bar{u}_p$	average velocity of particles within a fluid cell	m s^{-1}
V	velocity	m s^{-1}
V_{CS}^*	velocity the contact surface particle	—
V^*	non-dimensional velocity	—
V_{peak}^*	peak flow velocity in the velocity profile	—
$\partial_\chi V^*$	average gradient of flow velocity within the rear-surface flow acceleration region	—
$\partial_\chi V_{tail}^*$	rising rate within the rear-surface flow acceleration region	—
V_0^*	flow velocity at the front surface	—
$\tilde{V}$	interstitial gas velocity	m s^{-1}
V_{sc}	characteristic velocity scale	m s^{-1}
x	distance	m

Greek letters

Parameter	Explanation	Unit
α^2	averaged super particle loading	—
χ	non-dimensional distance	—
χ_{CS}	position of the contact surface	—
χ_{RSR}	beginning point of the rear-surface region across which the flow increasingly accelerates	—
χ_s	characteristic depth of the pressure diffusion	—
$\chi_{T_{max}^*}$	position the traversing hot gas layer reaching its maximum	—
$\chi_{T_{peak}^*}$	position of the temperature peak	—
$\chi_{\partial\rho>0}^0$	starting point of the region with positive density gradient	—
$\chi_{\partial\rho>0}^1$	ending point of the region with positive density gradient	—
$\Delta\chi_{\partial\rho>0}$	width of the region with positive density gradient	—
δ	overlap	m
ε	coefficient of restitution	—
ϕ_p	volume fraction of particles calculated through Voronoi tessellation	—
ϕ_0	initial volume fraction of particle column	—
γ	specific heat ratio	—
γ_n	damping coefficient	—

Parameter	Explanation	Unit
μ	dynamic viscosity	N s m^{-2}
ν	kinematic viscosity	m^2 s^{-1}
Π	infiltration coefficient incorporating both the properties of the quiescent gases and the structural properties of the granular column	—
θ	non-dimensional pressure	—
τ	non-dimensional time	—
τ_{diff}	characteristic time of the pressure diffusion	—
ξ_p	characteristic time ratio between isothermal and non-isothermal pressure diffusions	—
ξ_T	ratio between the traversing time of the hot gas layer and the characteristic time of the pressure diffusion	—

Subscripts

Symbol	Explanation
iso	isothermal case
non-iso	non-isothermal case

Declaration of interests. The authors report no conflict of interest.

Author ORCIDs.

Jiarui Li https://orcid.org/0000-0002-5148-7715;

Baolin Tian https://orcid.org/0000-0002-7929-8756;

Meizhen Xiang https://orcid.org/0000-0003-1666-9852;

Kun Xue https://orcid.org/0000-0002-2949-6498.

Appendix A. Parameters in each numerical case

Four primary variables are involved in our simulations: the Mach number of the incident shock, M_s, the particle diameter, d_p, the packing fraction of the particle column, ϕ_0, and the length of the column, l. With increasing Mach number from 1.094 to 2.986, the non-dimensional reflected shock intensity, N, introduced in (2.15) varies from 0.5 to 50. The other three variables constitute the filtration coefficient, Π. Since Π is mainly controlled by the particle diameter according to (2.18), d_p varies from 1 µm to 10 mm to ensure a wide variation range of Π. The packing fraction and particle column length contribute relatively less to Π; therefore, ϕ_0 and l only vary within narrow ranges, ϕ_0 from 0.45 to 0.58 and l/d_p from 200 to 1000. The exact values of the variable parameters in each case are provided in table 1.

Appendix B. Approach to obtain the trajectory of the contact surface

The trajectory of the contact surface, χ_{CS}, is the moving route of the first gas particle flowing into the granular column upon shock impingement which can be obtained from the gas velocity field shown in figure 9. The new position of this gas particle along the flow direction can be updated from its previous position and the corresponding local gas

N (M_s) / Π (d_p)	0.5 (1.09)	1 (1.17)	3.5 (1.43)	5 (1.54)	10 (1.83)	15 (2.04)	20 (2.22)	35 (2.65)	50 (2.99)
5000 (10 mm)	0.45–1000	0.45–1000	0.45–1000	0.45–1000	0.45–1000	0.45–1000	0.45–1000	0.45–1000	0.45–1000
50 (1 mm)	0.45–1000	0.45–1000	0.45–1000	0.45–1000	0.45–1000	0.45–1000	0.45–1000	0.45–1000	0.45–1000
0.5 (100 μm)	0.45–1000	0.45–1000	0.45–1000	0.45–1000	0.45–1000	0.45–1000	0.45–1000	0.45–1000	0.45–1000
0.045 (30 μm)	0.45–1000	0.45–1000	0.45–1000	0.45–1000	0.45–1000	0.45–1000	0.45–1000	0.45–1000	0.45–1000
0.005 (10 μm)	0.51–500	0.51–500	0.45–1000	0.45–1000	0.45–1000	0.45–1000	0.45–1000	0.45–1000	0.45–1000
4.5×10^{-4} (3 μm)	0.58–200	0.51–500	0.51–500	0.45–1000	0.45–1000	0.45–1000	0.45–1000	0.45–1000	0.45–1000
5×10^{-5} (1 μm)	0.58–200	0.51–500	0.51–500	0.45–1000	0.45–1000	0.45–1000	0.45–1000	0.45–1000	0.45–1000

Table 1. Exact values of the variable parameters in each numerical case. The Mach number, M_s, and corresponding shock intensity, N, are provided in the first row, while the particle diameter, d_p, and corresponding filtration coefficient, Π, are given in the first column. The packing fraction and the length of the particle column are represented in the following order: $\phi_0 - l/d_p$.
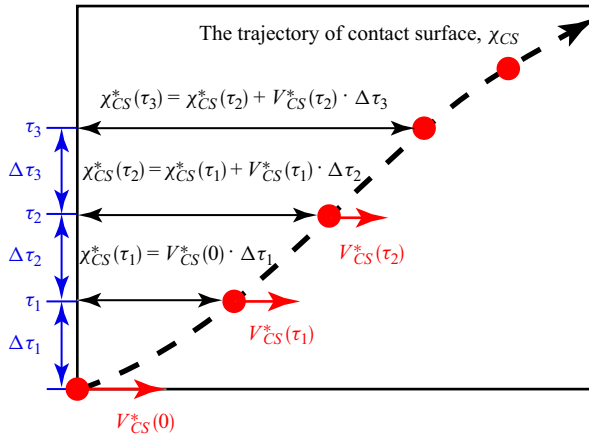
Figure 23. Schematic diagram of the process to obtain the trajectory of the contact surface.

velocity, as depicted in figure 23. Therefore, the complete trajectory of the contact surface is expressed as follows:

$$\chi_{CS}(\tau) = \int_0^\tau V_{CS}^* \, d\tau. \tag{B.1}$$

REFERENCES

ABIDOYE, L.K., KHUDAIDA, K.J. & DAS, D.B. 2015 Geological carbon sequestration in the context of two-phase flow in porous media: a review. *Crit. Rev. Environ. Sci. Technol.* **45**, 1105–1147.

ALOBAID, F. & EPPLE, B. 2013 Improvement, validation and application of CFD/DEM model to dense gas–solid flow in a fluidized bed. *Particuology* **11**, 514–526.

APTE, S., MAHESH, K. & LUNDGREN, T. 2003 A Eulerlan-Lagrangian model to simulate two-phase/particulate flows. Center for Turbulence Research Annual Research Briefs, pp. 161–171.

BAER, M.R. & NUNZIATO, J.W. 1986 A two-phase mixture theory for the deflagration-to-detonation transition (DDT) in reactive granular materials. *Intl J. Multiphase Flow* **12**, 861–889.

BALACHANDAR, S. 2012 Recent advances in compressible multiphase flows explosive dispersal of particles. In *Future Directions in CFD Research, a Modeling and Simulation Conference, Hampton*.

BDZIL, J.B., MENIKOFF, R., SON, S.F., KAPILA, A.K. & STEWART, D.S. 1999 Two-phase modeling of deflagration-to-detonation transition in granular materials: a critical examination of modeling issues. *Phys. Fluids* **11**, 378–402.

BEAR, J. & ALEXANDER, H.-D.C. 2010 *Modeling Groundwater Flow and Contaminant Transport*, 1st edn. Springer.

BEN-DOR, G., BRITAN, A., ELPERIN, T., IGRA, O. & JIANG, J.P. 1997 Experimental investigation of the interaction between weak shock waves and granular layers. *Exp. Fluids* **22**, 432–443.

BEN-DOR, G., MAZOR, G., IGRA, O., SOREK, S. & ONODERA, H. 1994 Shock wave interaction with cellular materials. *Shock Waves* **3**, 167–179.

BORCHARDT-OTT, W. 2012 *Crystallography: An Introduction*. Springer.

BRITAN, A., BEN-DOR, G., ELPERIN, T., IGRA, O. & JIANG, J.P. 1997 Gas filtration during the impact of weak shock waves on granular layers. *Intl J. Multiphase Flow* **23**, 473–491.

BRITAN, A., BEN-DOR, G., IGRA, O. & SHAPIRO, H. 2001 Shock waves attenuation by granular filters. *Intl J. Multiphase Flow* **27**, 617–634.

BRITAN, A., BEN-DOR, G., IGRA, O. & SHAPIRO, H. 2006 Development of a general approach for predicting the pressure fields of unsteady gas flows through granular media. *J. Appl. Phys.* **99**, 093519.

BRITAN, A., SHAPIRO, H. & BEN-DOR, G. 2007 The contribution of shock tubes to simplified analysis of gas filtration through granular media. *J. Fluid Mech.* **586**, 147–176.

BRITAN, A., SHAPIRO, H., LIVERTS, M., BEN-DOR, G., CHINNAYYA, A. & HADJADJ, A. 2013 Macro-mechanical modelling of blast wave mitigation in foams. Part I. Review of available experiments and models. *Shock Waves* **23**, 5–23.

CARMOUZE, Q., SAUREL, R., CHIAPOLINO, A. & LAPEBIE, E. 2020 Riemann solver with internal reconstruction (RSIR) for compressible single-phase and non-equilibrium two-phase flows. *J. Comput. Phys.* **408**, 109176.

CHIAPOLINO, A. & SAUREL, R. 2020 Numerical investigations of two-phase finger-like instabilities. *Comput. Fluids* **206**, 104585.

CHOI, D. & PARK, H. 2022 Flow–structure interaction of a starting jet through a flexible circular nozzle. *J. Fluid Mech.* **949**, A39.

CROWE, C.T., SCHWARZKOPF, J.D., SOMMERFELD, M. & TSUJI, Y. 2012 *Multiphase Flows with Droplets and Particles*. CRC Press.

DE PAOLI, M., ZONTA, F. & SOLDATI, A. 2016 Influence of anisotropic permeability on convection in porous media: implications for geological CO_2 sequestration. *Phys. Fluids* **28**, 056601.

DEL PRETE, E., CHINNAYYA, A., DOMERGUE, L., HADJADJ, A. & HAAS, J.F. 2013 Blast wave mitigation by dry aqueous foams. *Shock Waves* **23**, 39–53.

DI FELICE, R. 1994 The voidage function for fluid-particle interaction systems. *Intl J. Multiphase Flow* **20**, 153–159.

ERGUN, S. 1952 Fluid flow through packed columns. *Chem. Engng Prog.* **48**, 89–94.

ERIKSEN, F.K., TOUSSAINT, R., TURQUET, A.L., MÅLØY, K.J. & FLEKKØY, E.G. 2018 Pressure evolution and deformation of confined granular media during pneumatic fracturing. *Phys. Rev.* E **97**, 012908.

FENG, Y., XU, B., ZHANG, S., YU, A. & ZULLI, P. 2004 Discrete particle simulation of gas fluidization of particle mixtures. *AIChE J.* **50**, 1713–1728.

FLEKKØY, E.G., SANDNES, B. & MÅLØY, K.J. 2023 Shape of a frictional fluid finger. *Phys. Rev. Fluids* **8**, 114302.

FROST, D.L. 2018 Heterogeneous/particle-laden blast waves. *Shock Waves* **28**, 439–449.

GUBIN, S.A. 2018 Shock waves in porous media *J. Phys.: Conf. Ser.* **1099**, 012015.

GUO, Y., WASSGREN, C., HANCOCK, B., KETTERHAGEN, W. & CURTIS, J. 2015 Computational study of granular shear flows of dry flexible fibres using the discrete element method. *J. Fluid Mech.* **775**, 24–52.

GVOZDEVA, L., FARESOV, Y.M. & FOKEEV, V. 1985 Interaction between air shock wave and porous compressible material. *Sov. Phys. Appl. Math. Tech. Phys.* **3**, 111–115.

HAN, P., XUE, K. & BAI, C. 2021 Explosively driven dynamic compaction of granular media. *Phys. Fluids* **33**, 023309.

HAYEK, M. 2017 A model for subsurface oil pollutant migration. *Transp. Porous Media* **120**, 373–393.

HENDERSON, L., VIRGONA, R., DI, J. & GVOZDEVA, L. 1990 Refraction of a normal shock wave from nitrogen into polyurethane foam. *AIP Conf. Proc.* **208**, 814–818.

JI, S., LI, P. & CHEN, X. 2012 Experiments on shock-absorbing capacity of granular matter under impact load. *Acta Phys. Sin.* **61**, 184703–184703.

JIANG, Y., GUO, Y., YU, Z., HUA, X., LIN, J., WASSGREN, C.R. & CURTIS, J.S. 2021 Discrete element method-computational fluid dynamics analyses of flexible fibre fluidization. *J. Fluid Mech.* **910**, A8.

KAFUI, K.D., THORNTON, C. & ADAMS, M.J. 2002 Discrete particle-continuum fluid modelling of gas–solid fluidised beds. *Chem. Engng Sci.* **57**, 2395–2410.

KALENKO, S. & LIBERZON, A. 2020 Particle-turbulence interaction of high Stokes number irregular shape particles in accelerating flow: a rocket-engine model. *Intl J. Multiphase Flow.* **133**, 103451.

KONERU, R.B., ROLLIN, B., DURANT, B., OUELLET, F. & BALACHANDAR, S. 2020 A numerical study of particle jetting in a dense particle bed driven by an air-blast. *Phys. Fluids* **32**, 093301.

KRUGGEL-EMDEN, H., STURM, M., WIRTZ, S. & SCHERER, V. 2008 Selection of an appropriate time integration scheme for the discrete element method (DEM). *Comput. Chem. Engng* **32**, 2263–2279.

LAGE, J.L. 1998 The fundamental theory of flow through permeable media. From Darcy to turbulence. In *Transport Phenomena in Porous Media* (eds. D.B. Ingham & I. Pop), pp. 1–30. Pergamon.

LEVY, A., BEN-DOR, G., SKEWS, B.W. & SOREK, S. 1993 Head-on collision of normal shock waves with rigid porous materials. *Exp. Fluids* **15**, 183–190.

LI, J., XUE, K., ZENG, J., TIAN, B. & GUO, X. 2021 Shock-induced interfacial instabilities of granular media. *J. Fluid Mech.* **930**, A22.

LI, J., ZENG, J. & XUE, K. 2023 Pressure evolution in shock-compacted granular media. *Pet. Sci.* **20**, 3736–3751.

LIU, X., OSHER, S. & CHAN, T. 1994 Weighted essentially non-oscillatory schemes. *J. Comput. Phys.* **115**, 200–212.

MENG, B., ZENG, J., TIAN, B., LI, L., HE, Z. & GUO, X. 2019 Modeling and verification of the Richtmyer–Meshkov instability linear growth rate of the dense gas-particle flow. *Phys. Fluids* **31**, 074102.

MO, H., LIEN, F.S., ZHANG, F. & CRONIN, D.S. 2019 A mesoscale study on explosively dispersed granular material using direct simulation. *J. Appl. Phys.* **125**, 214302.

MORRISON, F.A. 1972 Transient gas flow in a porous column. *Ind. Engng Chem. Res. Fundam.* **11**, 191–197.

O'ROURKE, P.J. & SNIDER, D.M. 2010 An improved collision damping time for MP-PIC calculations of dense particle flows with applications to polydisperse sedimenting beds and colliding particle jets. *Chem. Engng Sci.* **65**, 6014–6028.

OSNES, A.N., VARTDAL, M. & PETTERSSON REIF, B.A. 2017 Numerical simulation of particle jet formation induced by shock wave acceleration in a Hele-Shaw cell. *Shock Waves* **28**, 451–461.

PATANKAR, N.A. & JOSEPH, D.D. 2001 Modeling and numerical simulation of particulate flows by the Eulerian-Lagrangian approach. *Intl J. Multiphase Flow* **27**, 1659–1684.

PATHAK, S. & SINGH, T. 2015 An analytic solution of mathematical model of boussinq's equation in homogeneous porous media during infiltration of groundwater flow. *J. Geogr. Environ. Earth Sci. Intl* **3**, 8.

PETEL, O.E., JETTÉ, F.X., GOROSHIN, S., FROST, D.L. & OUELLET, S. 2011 Blast wave attenuation through a composite of varying layer distribution. *Shock Waves* **21**, 215–224.

PETITPAS, F., FRANQUET, E., SAUREL, R. & LE METAYER, O. 2007 A relaxation-projection method for compressible flows. Part II. Artificial heat exchanges for multiphase shocks. *J. Comput. Phys.* **225**, 2214–2248.

PONTALIER, Q., LOISEAU, J., GOROSHIN, S. & FROST, D.L. 2018 Experimental investigation of blast mitigation and particle–blast interaction during the explosive dispersal of particles and liquids. *Shock Waves* **28**, 489–511.

QIAO, T., LIU, L. & JI, S. 2022 Superquadric DEM-SPH coupling method for interaction between non-spherical granular materials and fluids. *Particuology* **71**, 20–33.

RAM, O. & SADOT, O. 2015 Analysis of the pressure buildup behind rigid porous media impinged by shock waves in time and frequency domains. *J. Fluid Mech.* **779**, 842–858.

ROGG, B., HERMANN, D. & ADOMEIT, G. 1985 Shock-induced flow in regular arrays of cylinders and packed beds. *Intl J. Heat Mass Transfer* **28**, 2285–2298.

ROGUE, X., RODRIGUEZ, G., HAAS, J.-F. & SAUREL, R. 1998 Experimental and numerical investigation of the shock-induced fluidization of a particles bed. *Shock Waves* **8**, 29–45.

SADOT, O., RAM, O., BEN-DOR, G., LEVY, A., GOLAN, G., RAN, E. & AIZIK, F. 2013 A simple constitutive model for predicting the pressure histories developed behind rigid porous media impinged by shock waves. *J. Fluid Mech.* **718**, 507–523.

SAUREL, R., CHINNAYYA, A. & CARMOUZE, Q. 2017 Modelling compressible dense and dilute two-phase flows. *Phys. Fluids* **29**, 063301.

SHEN, H., HUANG, Y., ILLMAN, W.A., SU, Y. & MIAO, K. 2023 Migration behaviour of LNAPL in fractures filled with porous media: laboratory experiments and numerical simulations. *J. Contam. Hydrol.* **253**, 104118.

SKEWS, B. 1991 The reflected pressure field in the interaction of weak shock waves with a compressible foam. *Shock Waves* **1**, 205–211.

SKEWS, B.W. 2001 Shock wave propagation in multi-phase media. *Handbook of Shock Waves*, pp. 545–596. Academic Press.

SKEWS, B.W., ATKINS, M.D. & SEITZ, M.W. 1992 Gas dynamic and physical behaviour of compressible porous foams struck by a weak shock wave. In *Shock Waves* (ed. K. Takayama), pp. 511–516. Springer.

SMITH, P. 2010 Blast walls for structural protection against high explosive threats: a review. *Intl J. Prot. Struct.* **1**, 67–84.

SNIDER, D.M., CLARK, S.M. & O'ROURKE, P.J. 2011 Eulerian–Lagrangian method for three-dimensional thermal reacting flow with application to coal gasifiers. *Chem. Engng Sci.* **66**, 1285–1295.

SUNDARESAN, S., OZEL, A. & KOLEHMAINEN, J. 2018 Toward constitutive models for momentum, species, and energy transport in gas–particle flows. *Annu. Rev. Chem. Biomol. Engng* **9**, 61–81.

TIAN, B., ZENG, J., MENG, B., CHEN, Q., GUO, X. & XUE, K. 2020 Compressible multiphase particle-in-cell method (CMP-PIC) for full pattern flows of gas-particle system. *J. Comput. Phys.* **418**, 109602.

TORO, E.F. 2013 *Riemann Solvers and Numerical Methods for Fluid Dynamics || The HLL and HLLC Riemann Solvers*. Springer.

UKAI, S., BALAKRISHNAN, K. & MENON, S. 2010 On Richtmyer–Meshkov instability in dilute gas-particle mixtures. *Phys. Fluids* **22**, 104103.

VIVEK, P. & SITHARAM, T.G. 2019 *Granular Materials Under Shock and Blast Loading*, 1st edn. Springer.

XUE, K., MIU, L., LI, J., BAI, C. & TIAN, B. 2023 Explosive dispersal of granular media. *J. Fluid Mech.* **959**, A17.

XUE, K., SHI, X., ZENG, J., TIAN, B., HAN, P., LI, J., LIU, L., MENG, B., GUO, X. & BAI, C. 2020 Explosion-driven interfacial instabilities of granular media. *Phys. Fluids* **32**, 084104.

XUE, L., LI, D., NAN, T. & WU, J. 2019 Predictive assessment of groundwater flow uncertainty in multiscale porous media by using truncated power variogram model. *Transp. Porous Media* **126**, 97–114.

YAN, G., YU, H. & MCDOWELL, G. 2009 Simulation of granular material behaviour using DEM. *Procedia Earth Planet. Sci.* **1**, 598–605.

YIN, J., DING, J., LUO, X. & YU, X. 2019 Numerical study on shock–dusty gas cylinder interaction. *Acta Mechanica Sin.* **35**, 740–749.

YIN, L., NI, Z., LIU, J., FAN, F., ZHI, X., YE, J., PAN, Y. & GUO, Y. 2023 High-temperature mechanical properties of constructional 6082-T6 aluminum alloy extrusion. *Structures* **48**, 1244–1258.